

**ELECTRONIC AND ATOMIC PROCESSES IN
NANOWIRES**

A THESIS
SUBMITTED TO THE DEPARTMENT OF PHYSICS
AND THE INSTITUTE OF ENGINEERING AND SCIENCES
OF BILKENT UNIVERSITY
IN PARTIAL FULFILLMENT OF THE REQUIREMENTS
FOR THE DEGREE OF
MASTER OF SCIENCE

By

Hatem Mehrez
September 1996

THESIS
TK
3301
M44
1996

ELECTRONIC AND ATOMIC PROCESSES IN NANOWIRES

A THESIS

SUBMITTED TO THE DEPARTMENT OF PHYSICS
AND THE INSTITUTE OF ENGINEERING AND SCIENCE
OF BILKENT UNIVERSITY
IN PARTIAL FULFILLMENT OF THE REQUIREMENTS
FOR THE DEGREE OF
MASTER OF SCIENCE

Hatem Mehrez.

أحمد محمد مهrez

By
Hatem Mehrez
September 1996

TK

3301

·M44

1996

2035646

I certify that I have read this thesis and that in my opinion it is fully adequate, in scope and in quality, as a dissertation for the degree of Master of Science.



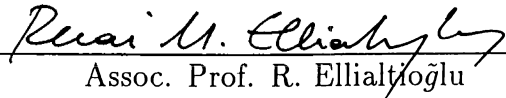
Prof. S. Ciraci (Supervisor)

I certify that I have read this thesis and that in my opinion it is fully adequate, in scope and in quality, as a dissertation for the degree of Master of Science.



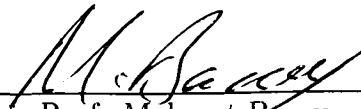
Prof. C. Yalbic

I certify that I have read this thesis and that in my opinion it is fully adequate, in scope and in quality, as a dissertation for the degree of Master of Science.



Assoc. Prof. R. Ellialtıođlu

Approved for the Institute of Engineering and Science:



Prof. Mehmet Baray,

Director of Institute of Engineering and Science

Abstract

ELECTRONIC AND ATOMIC PROCESSES IN NANOWIRES

Hatem Mehrez

M. S. in Physics

Supervisor: Prof. S. Ciraci

September 1996

The variation of conductance of a nanowire which is pulled between two metal electrodes has been the subject of dispute. Recent experimental set-ups using a combination of STM and AFM show that changes in conductivity are closely related with modification of atomic structure. In this thesis electron transport in the nanoindentation and in the connective neck are studied and features of measured conductance are analyzed. Molecular Dynamics simulations of nanowires under tensile stress are carried out to reveal the mechanical properties in nanowires in the course of stretching. A novel type of plastic deformation, which leads to the formation of bundles with “giant” yield strength is found. An extensive analysis on how abrupt changes in the conductance and the last plateau before the break are related with “quantization phenomena” and atomic structure rearrangements in the neck. By using *ab-initio* self-consistent field pseudopotential calculations we also investigated electron properties of nanowires and atomic chains and predicted the large yield strength observed in the center of connective neck.

Keywords:

conductance, nanowire, atomic structure, electron transport, nanoindentation, molecular dynamics, mechanical properties, bundles, self-consistent field, yield strength.

Özet

NANOTELLERDE ELEKTRON VE ATOM SÜREÇLERİ

Hatem Mehrez

Fizik Yüksek Lisans

Tez Yöneticisi: Prof. S. Ciraci

Eylül 1996

İki elektrot arasında çekilerek elde edilen nanotelde elektrik iletkenliğinin değişimi bilimsel bir tartışmaya yol açmıştı. STM ve AFM kombinasyonunu kullanan yeni deneysel düzenekler iletkenliğin değişiminin atomsal yapının değişimine bağlı olduğunu gösterdi. Bu tez çalışmasında STM uçu tarafından yapılan nanometre büyüklüğündeki batırmada ve bağlayıcı boyunda, elektron taşınımı konusu kuramsal olarak araştırılıp, ölçülmüş olan iletkenlik değerleri analiz edildi: Sünme esnasında nanotelin mekanik özelliklerini ortaya çıkarmak için gerilim altında Moleküler Dinamik benzeşimleri yapıldı. Çok büyük yığılma kuvvetine sahip atomsal lif yapısına yol açan yeni bir plastik şekil değişimi bulundu. İletkenlikte ani değişimlerin ve kopmadan önce son platonun kuvantum olayına ve atomsal yapı değişmesine nasıl bağlı olduğunun geniş bir açıklaması yapıldı. Kendi içinde tutarlı potansiyelimsi yöntemi kullanarak nanotellerin ve atom zincirlerinin elektriksel ve atomsal özellikleri ve bağlayıcı boyunun merkezinde yığılma kuvveti hesaplandı

Anahtar

Sözcükler:

İletkenlik, nanotel, atomsal yapı, elektron taşınımı, nano batırma, moleküler dinamik, mekanik özellikler, lifler, kendi içinde tutarlı, yığılma kuvveti.

Acknowledgement

I would like to express my greatest and endless thanks to my parents who have been waiting for a long time so that I can come up with this work.

I wish to express my deepest gratitude to Prof. S. Ciraci, my thesis supervisor. I wish to thank him very much for his fruitful discussions and suggestions; as well as for his challenging questions which has made me understand better what I am really doing. In addition to this I would like to thank him for helping me in solving even my own problems. He was really the most important person behind this work.

It is also a pleasure to acknowledge Dr. Erkan Tekman, Dr. Şakir Erkoç, Dr. Bilal Tanatar and Dr. Ziya Guvenç. for their valuable discussions, continuous help and morale support.

I would like to thank all the members of physics department at Bilkent University who have helped me in the course of this study and in fact during all my life at Bilkent university.

Finally I would express great thanks to my friend Ahmed Ben Halima who have helped me while writing my thesis. Also the deepest, greatest and endless thanks are given to my dearest Leyla Öz for her patience, understanding, morale support and great help during my M.S study.

Contents

Abstract	i
Özet	iii
Acknowledgement	v
Contents	vi
List of Figures	viii
1 Introduction	1
1.1 Problem development	1
1.2 Experiments on Long Quantum Wires	9
1.3 Theories	14
2 Ballistic transport through 3D QPC	16
2.1 Theory and general formalism	16
2.2 Cylindrical Infinite Well Confinement	24
2.2.1 Formalism	24
2.2.2 Results	29
2.3 Parabolic Potential Confinement	34
2.4 Nonuniform constriction	35
2.4.1 Transfer Matrix Method	35
2.4.2 Nanoindentation	39
2.4.3 Resonant Tunneling	42

3	Yielding and Fracture Mechanics ...	44
3.1	Motivation	44
3.2	Molecular Dynamics Simulation	45
3.2.1	Investigated Parameters	45
3.2.2	Molecular Dynamics Method	48
3.3	Results and Discussion	50
3.3.1	Nanowire <i>WN1</i>	50
3.3.2	Nanowire <i>WN2</i>	57
3.3.3	Nanowires <i>TN</i>	60
3.3.4	Nanowires <i>WN3</i>	63
4	SCF Pseudopotential Calculations	66
5	Conclusion	73

List of Figures

1.1	Jump to atom point contact in STM experiment	2
1.2	Experimental set up for <i>2DEG QPC</i> experiment	3
1.3	Conductivity in <i>2DEG QPC</i>	4
1.4	Experimental set up for MCBJ	10
1.5	Some experimental results on long quantum wires	11
1.6	Experimental results on Pt nanowire	12
1.7	Experimental results on Pb nanowire	13
2.1	Conductance for semiinfinite cylindrical constriction	31
2.2	Conductance for some finite length cylindrical constriction	32
2.3	Conductance for finite length constriction with parabolic confinement	34
2.4	Conductance during an indentation of a tip	41
2.5	Conductance for various potential confinement	42
3.1	Description of different structures used in the simulation.	48
3.2	Force of attraction in <i>WN1</i> structure	50
3.3	Side view of the neck atoms at some specific stretch increments $m\Delta l$	51
3.4	Lateral view at different stretch increments for structure <i>WN1</i>	54
3.5	Recovering of lateral layer structure <i>WN1</i> at certain stretch points	55
3.6	Formation of bundle structure at the neck for <i>WN1</i>	56
3.7	Force of attraction in <i>WN2</i> structure	57
3.8	Side view of the neck atoms at some specific stretch increments $m\Delta l$ for <i>WN2</i>	58
3.9	Formation of bundle structure at the neck for <i>WN2</i>	60

3.10	Force versus stretch for $TN2$ nanowire at $T=300K$ and $T=1K$. .	62
3.11	Force versus Stretch increment $m\Delta l$ for nanowire $WN3$ at $T = 300 K$	63
4.1	Band structure for Al and Na chains	67
4.2	Probability density distribution in Al $1D$ chain	68
4.3	Energy band structure for Al neck	70
4.4	Probability density distribution in Al neck	71

Chapter 1

Introduction

1.1 Problem development

Material systems of reduced size or dimensionality are of great interest, because they often do exhibit properties that are very different from those of the bulk material; among these, we state localization phenomena in low dimensional systems,¹ mechanical properties characterized by a reduced propensity for the creation and propagation of dislocations in small metallic samples² and quantized conductance in point contacts which will be the focus of this study.

The first step for the discovery of conductance quantization is due to the seminal Scanning Tunneling Microscopy (STM) works of Gimzewski and his collaborators,³ who have investigated tip-sample separation distance in a controlled manner over an extended range and they could observe clearly transition from the tunneling regime to the point contact. In Figure 1.1 we show the results obtained by Gimzewski *et al.* for the current I versus distance between the tip and surface. In Figure 1.1-a, the jump from the tunneling regime to the Quantum Point Contact (QPC) is represented by arrow at C and in Figure 1.1 - b, where current versus pushing and retraction is drawn, plateau structure is revealed.

Independently from this work, some experimental set-ups were developed in order to study this process in two dimensional electron gas (2DEG). The

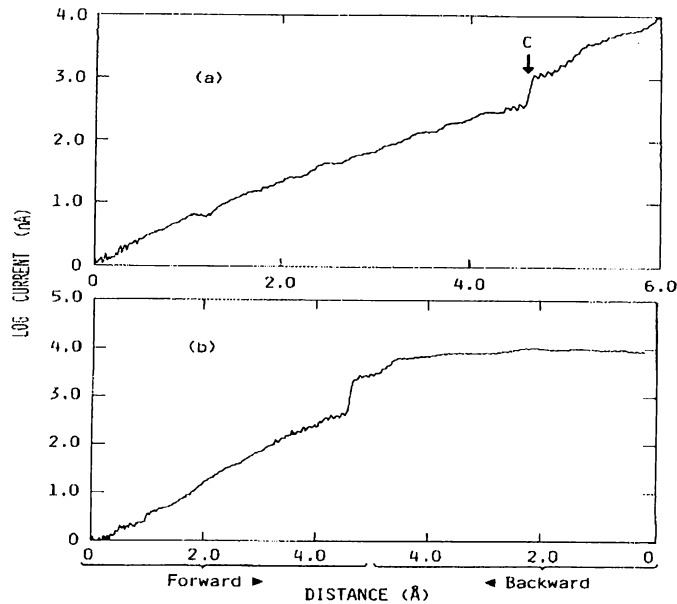


Figure 1.1: Tunneling current versus distance z for a clean iridium tip and polycrystalline Ag surface: (a) approach ($V_t = 20\text{mV}$), (b) approach and retraction ($V_t = -2\text{mV}$).[Ref.3]

pioneering works have been reached by van Wees *et al.*⁴ as well as Wharam *et al.*,⁵ who were able to see quantum conductance phenomenon with an error less than 5%. That has been a break-through in the field of ballistic transport in mesoscopic physics. The experimental set-up which introduced the quantization of conductance in *2DEG* is shown in Figure 1.2. In this system, point contacts are made on high-mobility molecular-beam-epitaxy-grown *GaAs/AlGaAs* heterostructure. The *2DEG*, which is formed at the interface between *GaAs* and *AlGaAs* slabs has mobility $\sim 100\text{m}^2\text{V}^{-1}\text{s}^{-1}$ and density $\sim 10^{15}/\text{m}^2$ so that the Fermi wave length $\sim 100\text{\AA}$.

On the top of the heterostructure, a metal gate is made with an opening \sim few λ_F (Fermi wave length) and much smaller than l_e (mean free electron path). The point contacts are defined by applying a negative voltage V_g to the gate. For small V_g , the *2DEG* (formed at the interface between *GaAs* and *AlGaAs*) which is underneath the gate is depleted and the conduction is taking place at the contact only with width $w \sim$ opening of the gates; by further decreasing of

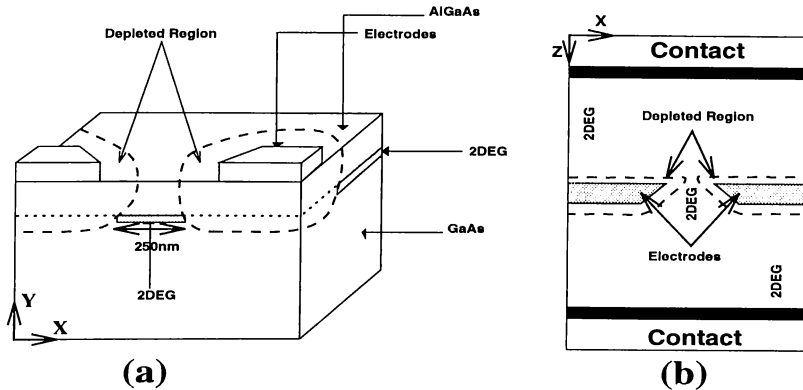


Figure 1.2: Schematic Diagram of 2DEG Quantum Point Contact, (a) lateral cross-section view and (b) top view.

V_g , the depletion layer increases and the width of the point contacts is reduced gradually until it is pinched off completely. Therefore, with this novel device, we can vary the width of the *QPC* for a given device configuration by changing V_g only.

With this device, two terminal resistance of several point contacts as a function of gate voltage was measured^{4,5} and in Figure 1.3 we show the experimental results of van Wees *et al.*⁴ after contact resistances are subtracted. It is clear from the graph that the conductance of the *QPC* as a function of V_g changes in the form of a stair-case with steps of $2e^2/h$ within a precision of few percent.

These experimental results have brought a new insight to the physics of *QPC* which was known as early as the mid 60's; Sharvin⁶ has calculated the conductance of a point contact using Drude approximation and found it to depend on the Fermi energy of the system and its geometry through the relation

$$G_s = \frac{2e^2}{h} \frac{A}{\lambda_F} \quad (1.1)$$

where A is the contact area for 3D point contacts and slit opening for 2D.

Eventhough the results in Figure 1.3 are in agreement with the Sharvin's approximation for conductivity; i.e, $G \sim w$, the jumps in the conductivity are not consistent with the constant slope for the G_s versus w curve of Sharvin's conductivity. In fact this main difference in conductivity between the

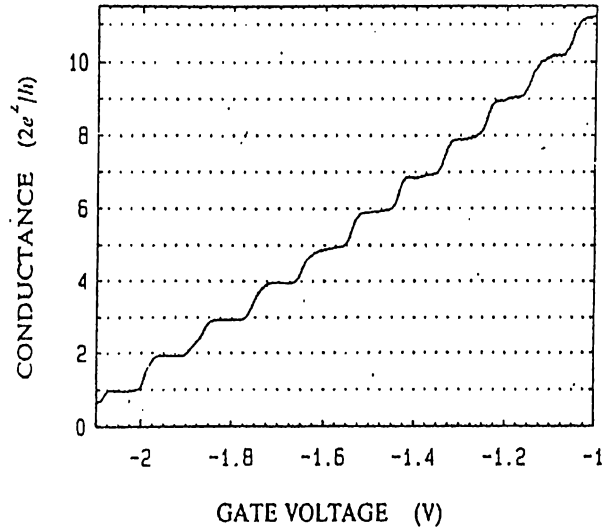


Figure 1.3: Conductivity v.s Gate voltage for *2DEG* which shows clearly the conductivity quantization. Ref[4]

experimental results and the G_s is due to dimensional effects. In Sharvin's study (and early approaches), point contacts scale length $L_z \ll \lambda_F$, and as a result, quantization effect due to the constriction width w is smeared out mainly due to the tunneling phenomenon; therefore in early studies quantization effect was not taken into consideration. However, with these new experimental results, a more detailed solution need to be carried out to show the quantum size effects, and this was cleared up^{4,5} in terms of the subband formation which was explained earlier.⁷

In order to understand this phenomenon better, we consider the following simple derivation. At the interface between the two slabs *GaAs* and *AlGaAs*, the *2DEG* is constrained to a certain well along the (x, y) direction due to the depletion generated by the negative gate voltage, but it is free to move along the channel (z) direction. Therefore we can represent the potential confinement by

$$V(x, y, z) = \begin{cases} 0 & \text{for } 0 < x < L_x \text{ and } 0 < y < L_y \\ \infty & \text{otherwise} \end{cases} \quad (1.2)$$

The solution to this problem is quite simple and we can separate the wave function to lateral part (in the x and y direction) and longitudinal one (in the z direction),

and we will get energy eigenvalue

$$E = E_{x,y} + \frac{\hbar^2 \vec{k}_z^2}{2m} \quad (1.3)$$

where \vec{k}_z is the propagation vector along the z -axis.

On the (x, y) plane, we have approximated our potential as a quantum well with an infinite wall barrier and this would yield the vanishing of the wave function at the boundaries giving rise to only some possible eigenfunctions to the problem with eigenenergy spectrum

$$E_{x,y} = E_{n_x, n_y} = \frac{\hbar^2}{2m} \left[\left(\frac{n_x \pi}{L_x} \right)^2 + \left(\frac{n_y \pi}{L_y} \right)^2 \right] \quad (n_x \neq 0 \text{ and } n_y \neq 0) \quad (1.4)$$

where n_x and n_y are quantum numbers describing eigenfunction solution and L_x and L_y are the width of the channel and accumulation layer respectively as shown in Figure 1.2.

We note here that $L_y \ll L_x$, therefore many eigenstates corresponding to different n_x values and $n_y = 1$ would have a lower energy eigenvalue compared to the state with $n_y = 2$; as a consequence, we can disregard the y dependence of the solution by assuming that only $n_y = 1$ are the filled states of the system, so the energy of the system is

$$E = \frac{\hbar^2}{2m} \left(\frac{n_x \pi}{L_x} \right)^2 + \frac{\hbar^2 \vec{k}_z^2}{2m} \quad (1.5)$$

where the constant energy $\hbar^2/(n_y \pi/L_y)^2/2m$ is taken to be zero by changing the reference of energy spectrum.

Connecting the channel to two reservoirs with Fermi energy E_F at $z = \pm\infty$ and keeping it at constant and small chemical potential difference $\Delta\mu$, we can find the conductance of this *QPC* through the relation $G = I/V$. In order to find the current I , we will use the relation

$$I = ev_F D(E_F) \Delta\mu \quad (1.6)$$

where v_F is the Fermi velocity, $D(E_F)$ the density of states at Fermi level and $\Delta\mu$ is the chemical potential. For the multiple subbands case, we will have

$$I = e \sum_{n_x} v_{n_x}(E_F) D_{n_x}(E_F) \Delta\mu \quad (1.7)$$

where n_x is the subband index. Assuming no subband interaction occurring in such a system, the generalization of the *one* band system gives

$$D(E) = \frac{\sqrt{2m}}{hE^{\frac{1}{2}}} \text{ (with spin degeneracy and positive } \vec{k}_z \text{)} \quad (1.8)$$

$$v(E) = \sqrt{\frac{2}{m}} E^{\frac{1}{2}} \quad (1.9)$$

We note here that we have taken only electrons in the energy range E_F and $E_F + \Delta\mu$ (only these ones contribute to the effective current) and with positive \vec{k}_z in the calculation of $D(E)$ because the ones with negative \vec{k}_z do not enter the channel and they do not yield any current contribution to the system. Therefore

$$I = \sum_{n_x} \Theta(E_F - E_{n_x}) \frac{2e}{h} \Delta\mu \quad (1.10)$$

where $E_F - E_{n_x} = \frac{\hbar^2 \vec{k}_z^2}{2m}$ is the longitudinal energy of the electrons in n_x band which has to be positive to be a current carrying state. Since $\sum_{n_x} \Theta(E_F - E_{n_x}) = N \equiv$ total number of bands with energy E below E_F so

$$I = \frac{2e}{h} \Delta\mu N \quad (1.11)$$

Thus

$$G = \frac{I}{V} = \frac{2e}{h} \frac{\Delta\mu}{V} N = \frac{2e}{h} \frac{eV}{V} N = \frac{2e^2}{h} N \quad (1.12)$$

Obviously we can understand better the staircase structure shown in Figure 1.3. As the gate voltage is increased, the depletion layer decreases allowing more states dipping below the Fermi energy and every state would contribute to 1 “quantum conductance” ($2e^2/h$). Therefore, we can explain every step in conductivity graph of Figure 1.3 by dipping one more state below the Fermi level.

Eventhough this theoretical derivations made us understand better the experimental results, further investigations of the approximations need to be carried out to understand the applicability of the theory and this would include tests on the following parameters

- The potential profile, which is assumed to be a perfect quantum well ignoring any variations which may occur due to surface roughness.
- Contacts occur at the $z = \pm\infty$ and this would prohibit any tunneling or reflections at the boundary edges of the channel.
- Band mixing is ignored and this is true only at $T = 0K$ and at perfectly smooth surface.

The effect of the confining potentials has been the object of detailed calculations.⁹⁻¹⁴ In these calculations, it was shown that for long constriction ($L_z \gg \lambda_F$), the conductance is directly proportional to integer number of propagating modes or conductance channels and increases with increasing width of constriction in steps of $2e^2/h$ when a new channel opens up. Even in the case of constriction length $L_z \sim \lambda_F$, the conductance still show staircase structure with oscillatory behavior.¹³ However in the case of very short constrictions ($L_z \ll \lambda_F$) where tunneling becomes important in such systems and the stair-case form is smeared out, and we approach G_s curve as $L_z \rightarrow 0$.

Based on these theoretical studies, we can conclude that, the potential profile or surface roughness itself does not change the general feature of the G curve since any potential profile which yields quasi bound states give rise to such jumps in the conductivity whenever a new bound state dips below the Fermi energy. However the length of the channel plays an important role in these calculations, since shorter constrictions cause more reflections of the eigenstates at the boundaries of the channel and these would introduce oscillations on the plateaus¹⁵ of conductivity and, for $L_z \ll \lambda_F$, tunneling phenomenon becomes pronounced and stair-case structure starts to disappear reaching Sharvin curve for $L_z \sim 0$.

Temperature dependence on conductivity in many subband system was studied throughly by M. Büttiker *et al.*¹⁶ and they found a generalization of Landauer's formula⁸ at finite T . Another approach was used by Tekman and Ciraci,¹³ who have used the variation of $D(E)$ at finite T in equation 1.7, while calculating the current I , and they found that for very thin constrictions

($L_x \sim 2\lambda_F$) where the energy difference between energy eigenvalues are quite large compared to the case of wide openings, temperature effects are quite small up to $T = 5K$ and they just diminish oscillations occurring at the plateaus. However, for the case of large openings ($L_x \sim 10\lambda_F$), the inter subband mixing becomes very important and the stair-case structure disappears for $T > 0.6K$. Within these theoretical calculations, based on free electron model and an approximate potential profile confinement, it is generally accepted that this model explains well the *2DEG* experimental results, except for the resonance structure superposed on the plateaus which is due to reflections from the ends of the channel and was not detected experimentally.

Coming back to the work done by Gimzewski and Möller³ in which tunneling current exhibits a jump and saturates as the tip is brought closer to the sample at a certain tip-sample separation distance. If we use the results of this experiment and plot G versus tip displacement, a plateau would show up. Analysis has shown that the discontinuous jump is due to the adhesion of the tip to the sample, which happens when the tip-sample system is unstable at certain separation. In this case the tip elongates towards the sample and forms a mechanical contact in the form of a neck as shown schematically by Gimzewski *et al.*³ They have estimated the contact radius to be $\sim \lambda_F$. Therefore, length in such systems is of the order of λ_F , and the observed transport beyond the discontinuity in Figure 1.3 has to be associated with ballistic quantum transport. As a result it would be possible to generalize the theory applied to the *2DEG* to this system. Garcia¹⁷ was the first one who pointed out that the point contact in STM is related to ballistic transport of electrons through *QPC*. Following these predictions, Lang¹⁸ has simulated the point contact experiment by two jellium electrodes, one of them having an adsorbed Na atom on it and thus representing a single atom tip. He found that the conductance saturates at a value of $\eta 2e^2/h$ and forms a plateau, where the value of η depends strongly on the identity of the material and it is only 0.4 for Na. Different approach was used by Ferrer *et al.*¹⁹ who have studied contact resistance of STM at a very small separation using tight-binding Hamiltonian and Keldysh (non-equilibrium) Green's function formalism

and they have found that the conductivity saturates at close contact $\sim 2.5\text{\AA}$ to a value $\sim 2e^2/h$. In parallel with these two different approaches, Ciraci and Tekman²⁰ have studied the transition from tunneling regime to point contact in STM within Self-consistent-field (SCF) pseudopotential method and they found that the variation of G as a function of tip-sample separation is sample and tip specific. Moreover, they have explained the observed jumps of G by the irregular enlargement of the contact area. Nevertheless, we can state that the step structure can also be revealed in 3D QPC , which seems to be explained by using ballistic theory. In treating the experimental results of Gimzewski *et al.*,³ we should note that the diameter of the neck is $\sim \lambda_F$; as it is already concluded in the theoretical studies,¹³ that we can not really expect sharp quantization in such experiments.

1.2 Experiments on Long Quantum Wires

Recently, by pulling the tip after nanoindentation²¹⁻²⁴ or by using a mechanically controllable break junction system (MCBJ)²⁵⁻²⁷ long metal wires with diameters in the range of a few λ_F have been produced. As the cross-section of the wire is reduced by stretching it continuously, the two-terminal conductance G has been measured. In Figure 1.4 we show the schematic description of a MCBJ taken from reference 25. Referring back to this figure, the sample in the shape of a metal filament is glued on a substrate (bending beam), then by bending the substrate in high vacuum, the filament is broken. The electrodes, which are thus freshly exposed, are brought back into contact. The bending which is controlling the separation distance between the ends of the wire is controlled by tuning the piezo voltage V_p allowing fine adjustment of the separation between the electrodes. In the STM experiment, the tip is pushed into the surface beyond the separation distance at which the jump to QPC occurs and then it is slowly retracted yielding to a long neck formation²⁴ of $\sim 40\text{\AA}$.

Eventhough the experimental set-up of the STM and MCBJ are different, the principle of neck formation is the same: stretching a material with a small contact

area of $\sim 10\text{\AA}$ and measuring its two terminal conductance G . In fact these experiments have been done on a variety of materials and here we will show some experimental results and make some comments on them.

In Figure 1.5, we show some experimental results obtained from Cu, Al, Na and Au. The conductivity in the first three plots were measured by MCBJ while that of gold was measured with STM set up. From these plots, we can recognize some interesting features occurring in the conductivity measurements which are absent in Figure 1.3 showing the quantization in *2DEG*. The most important differences include

- STM and MCBJ give the same general graph features for the conductivity.
- Results for Na (in Figure 1.5-c) show clearly that these experiments are quite irreproducible apart from the last plateau which survives for a longer time interval compared to the other ones.

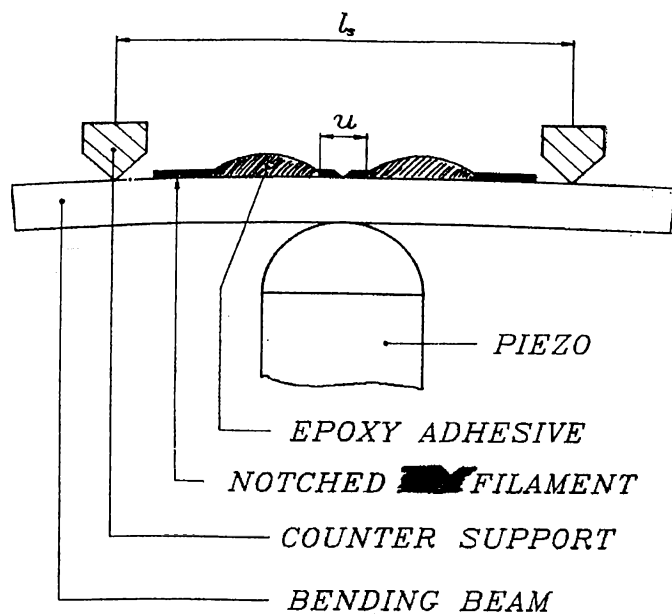


Figure 1.4: Schematic diagram for mechanically controllable break junction. Ref.[25]

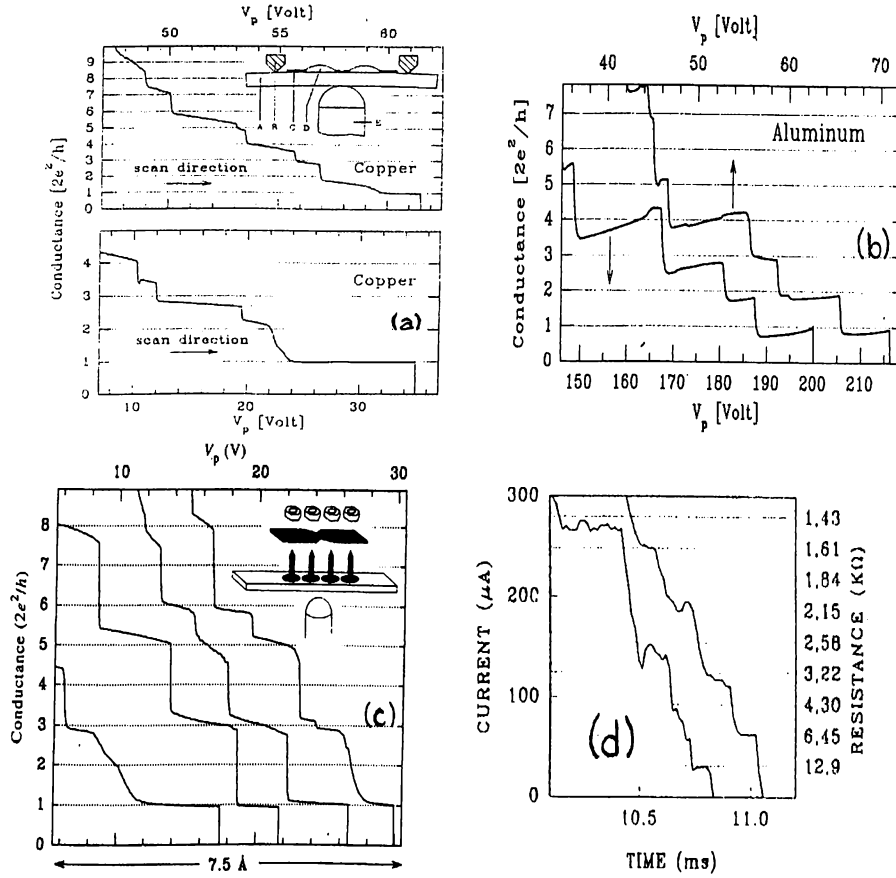


Figure 1.5: Conductivity in metal neck structures. (a), (b) and (c) are measured with MCBJ set up for Cu, Al and Na respectively at 1.3K as a function of V_p (piezo voltage). (d) is Au conductivity measurement with STM set up as a function of time before the neck breaking. Ref[25,22,26]

- For $G > 5G_o$ ($G_o = 2e^2/h$) plateau structure starts to smear out and we are in fact very close to Sharvin case.
- Plateaus may have jumps of $\sim G_o$ or $\sim 2G_o$.
- For Al and Au (Figure 1.5-b,d), we can see some dipping phenomena in the conductivity measurement at the beginning of every lower plateau.
- For the Al wire, we can also observe a small increase in the conductivity before the neck is broken.

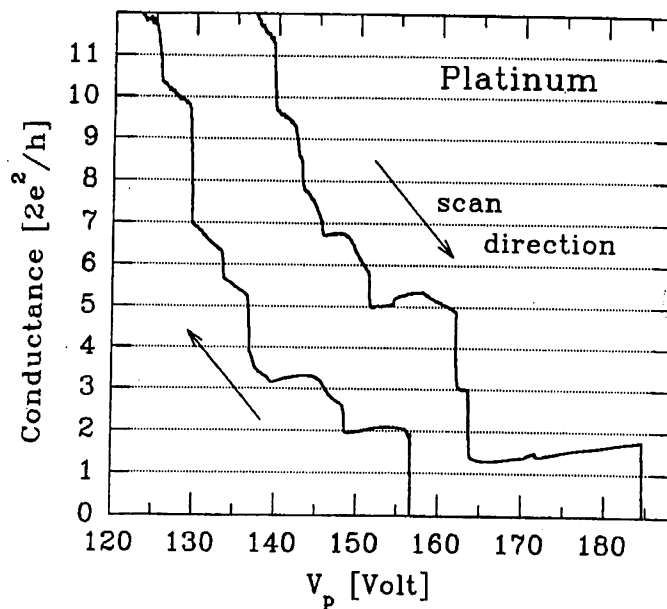


Figure 1.6: The conductance of a Pt junction at $1.3K$ as a function of V_p for two successive scans. In the first scan the transition was approached from the contact side whereas in the second scan the transition was approached from the tunnel side. Ref[24]

Eventhough, metals are the best materials to be described by free electron model and as a result our generalization of quantization phenomenon would work best in such a system, we can see from the previous remarks that $3D QPC$ features differs from those of $2DEG$. As a result simple generalization of the previous theory would most probably fail. In fact investigating other types of materials, such as transition metals (Pt) or semi-metals (Sb), shows well that this “quantization” phenomenon is quite fragile and it is too much material dependent. In Figure 1.6, we show the graph for Pt conductivity which exhibits the formation of plateaus, but quite different from the ones shown previously. In this Figure, we also note that

- The last plateau corresponds to a conductivity of $2G_o$.
- The slope of the last plateau becomes much more pronounced relative to that of Al.

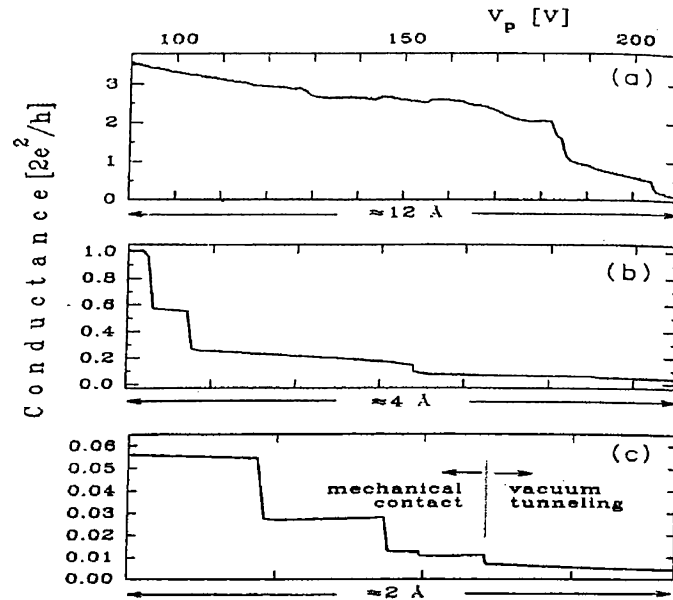


Figure 1.7: Three examples of conductance of a Sb contact at $1.3K$ as a function of V_p , with V_p increasing. The three curves are recorded for three different V_p sweeps. Curve (a) shows the behavior for a large decreasing contact size. In the mechanical contact regime shown in curve (c) as well as in curve (b), the conductance is less than the quantum unit. Ref[27]

- Hysteresis effect becomes much more important for this structure.

Concerning the results of semimetals, where we have taken Sb as an example, we show the variation of conductance in Figure 1.7. Here we can observe the following important feature

- “Quantization” phenomenon becomes nearly impossible to explain the plateaus which still occur but they exhibit jumps with a small fraction of $2e^2/h$.

Within these new experimental results, it has become quite difficult to explain this “random” plateau formation with a simple generalization of the theory applied to $2DEG$. Hence, for the last three years the problem has been revisited with the hope of resolving this quantization phenomenon.

1.3 Theories

It has been suggested that these plateaus occurring in the conductance in the *QPC* regime are due to discontinuous change of atomic structure,^{13,28,29} and every atom at the narrowest part of the neck opens a channel when one of its states ϵ_a is in common with the Fermi level. Even if ϵ_a is above the E_F , ballistic transport may still occur because the state is broadened and becomes a resonance³⁰ centered at

$$\epsilon = \epsilon_a + \Lambda \quad (1.13)$$

with FWHM Γ , and has density

$$\rho_a(\epsilon) = \Delta/\pi[(\epsilon - \epsilon_a - \Lambda)^2 + \Gamma^2]^{-1} \quad (1.14)$$

The distribution $\rho_a(\epsilon)$ may have a partial overlap with the Fermi level and hence the conductance over this resonance may be smaller than G_o . Therefore, the total conductivity of the neck would be the sum of individual atom contributions which are at the neck. On the other hand, still there are some who believe that this sharp step structure indicates the unique transversal quantization along the *3D* constriction,^{22,23,31} and they assume that the energy states vary adiabatically so that the channel mixing due to finite bias, temperature and saddle point potential is marginal. The height of each step is equal to n -multiple of G_o , where n being the degeneracy of the corresponding state below E_F . In addition to this, marginal differences from “quantum” conduction could be well explained through scattering phenomenon due to potential variations at the neck. Until today, both views are still a matter of dispute between different groups³² and the quantization of conductance in atomic wires is not completely resolved.

In order to understand better the quantization phenomenon, we have decided to make a study on the atomic and electronic properties of these nanostructures. Firstly, we will treat our system with free electron model in the ballistic regime. In the next chapter, we will show our conductance calculation for different neck profiles in order to grasp the effect of quantization phenomenon in small systems. Following this, we will make a detailed atomic structure analysis for

neck samples while pulling. Because in small systems such as atomic scale wires, the mechanisms of deformation and hence propensity for the creation and propagation of dislocations is reduced.² The structural changes occurring in such systems are quite different from the bulk material and for this reason we have made simulations with Molecular Dynamics³³(MDS) on small structures to understand structural deformation in them and attempted to investigate the control parameters including: pulling rate, temperature, crystal structure and interaction potential type. This study will be presented in chapter 3. In chapter 4 we will introduce Self-Consistent-Field (SCF) calculations for different neck samples and infinite wires in order to understand the physical difference between the finite and infinite size nanostructures. Finally in the concluding section we address to the questions we raised while analyzing experimental results on the *3D QPC* with the hope of providing better understanding.

Chapter 2

Ballistic transport through 3D

QPC

2.1 Theory and general formalism

We have seen in Chapter 1 that in the 2 *DEG*, quantization phenomenon of 2D *QPC* is due to the *quasi* – 1D nature of the system, and there were many theoretical studies devoted to explain this phenomenon. Now we would generalize the formalism¹³ which has been applied by Tekman and Ciraci.

In this approach we will divide the space into three parts: 1) the left most and 2) right most parts are two semiinfinite jellium electrodes, so the Shrödinger equation in this portion of space would simply give a free plane wave particle solution. 3) the central part of the constriction which is characterized by a laterally confining potential, and as a result, the solution of the Shrödinger equation in this region are subband wave functions arising from the quantization of the transverse momentum. The separation of space into jellium electrodes and constriction can be represented by using profile confinement $V(x, y, z)$ defined by

$$V(x, y, z) = [\phi_m(z) + V_c(x, y, z)]\theta(z)\theta(d - z) \quad (2.1)$$

where θ is the step function and d is the constriction length; here the potential is taken zero in the left most ($z < 0$) and right most ($z > d$) regions, while

at the constriction ($0 < z < d$), the potential has two parts, the longitudinal part $\phi_m(z)$ (which contains the variation of minimum value of potential along the constriction) and the confining part $V_c(x, y, z)$ (which gives rise to subband structure). For a general constriction, it may not be obvious and may even not be unique to decompose the potential $V(x, y, z)$ to this type of confining model, however, in nearly free electron approximation,^{13,34} the 3D potential of contact is obtained from SCF calculations and is parameterized

$$V(x, y, z; d) = \phi_m(z; d) + \alpha(z; d)(x^2 + y^2) \quad (2.2)$$

here x and y are transversal coordinates and z is the longitudinal coordinate from left electrode towards the right electrode along the axis of contact; while d is the constriction length.

The hamiltonian for the QPC is written as

$$H = -\frac{\hbar^2}{2m^*} \nabla^2 + V(x, y, z) \quad (2.3)$$

where m^* is the effective mass[¶] of the electron propagating through the constriction and it is assumed to be isotropic. Therefore Shrödinger equation would have the form

$$\left[-\frac{\hbar^2}{2m^*} \frac{\partial^2}{\partial z^2} + \phi_m(z) - \frac{\hbar^2}{2m^*} \nabla_{\parallel}^2 + V_c(x, y, z) \right] \psi_{n,E}(x, y, z) = E \psi_{n,E}(x, y, z) \quad (2.4)$$

where $\nabla_{\parallel}^2 = \partial^2/\partial x^2 + \partial^2/\partial y^2$, the term n corresponds to the subband wave function induced due to the confining potential $V_c(x, y, z)$ and the energy is assumed to be continuous due to the propagation along the z axis. We note here, that the solutions of Shrödinger equation are two-fold degenerate; if $\psi_{n,E}(x, y, z)$ is a solution of equation 2.4 with left current carrying state, then $\bar{\psi}_{n,E}(x, y, z)$ is also a solution and corresponds to the state which carries current in the opposite direction.

[¶]In our calculations, we would use effective mass theory which treats the effect of the atoms potential as renormalization of the free electron propagation energy. Our approximation is justified because our system size contains a large number of atomic cells and the external potential is slowly varying over atomic scale length.

The solution of the equation 2.4 is not always possible, because generally the partial differential equation is not separable. Then we have to deal with solutions only for very special potential confinements in section 2.2 and approximate solutions for a general confinement is applied in section 2.3. However, for the time being we would suppose the subband wave functions $\psi_{n,E}(x, y, z)$ and $\bar{\psi}_{n,E}(x, y, z)$ are well known in the constriction and will find the conductance for such a system.

Assuming that the subband wave functions in the constriction are known, the general solution of the Shrödinger equation in all space is found by matching these solutions with the plane wave nature of the wave functions at the jellium electrodes ($z < 0$ and $z > d$). To this end the following conditions have to be satisfied

- Continuity of the wave function and its derivative at the left boundary of the constriction ($z = 0$).
- Continuity of the wave function and its derivative at the right boundary of the constriction ($z = d$).
- Boundary condition at $z = \pm\infty$ which define incoming and outgoing waves.

Let us consider an incident plane wave from the left hand side of the constriction with wave vector $\vec{K}_i = (\vec{k}_{x_o}, \vec{k}_{y_o}, \vec{k}_{z_o})$, \vec{k}_{z_o} is in the longitudinal direction, \vec{k}_{x_o} and \vec{k}_{y_o} are in the lateral direction, and its energy $E = \hbar^2 |\vec{K}_i|^2 / 2m^*$. Since in this problem, we are assuming that the characteristic length of the constriction is smaller than the electron mean free path i.e the contact is ballistic; therefore plane waves at the left most and right most sides and at the constriction have the same energy E and we will write the wave functions as

$$\begin{aligned}
 \Psi_{\vec{K}_i}(x, y, z) &= e^{ik_{z_o}z} e^{ik_{y_o}y} e^{ik_{x_o}x} + \int dk_x dk_y e^{-ik_z(k_x, k_y)z} e^{ik_x x} e^{ik_y y} A_{\vec{K}_i}(k_x, k_y) \quad (z < 0) \\
 &= \sum_n \left\{ \psi_{n,E}(x, y, z) \Theta_{n, \vec{K}_i} + \bar{\psi}_{n,E}(x, y, z) \Delta_{n, \vec{K}_i} \right\} \quad (0 < z < d) \quad (2.5) \\
 &= \int dk_x dk_y e^{ik_z(k_x, k_y)z} e^{ik_x x} e^{ik_y y} B_{\vec{K}_i}(k_x, k_y) \quad (z > d)
 \end{aligned}$$

where the first term of equation 2.5 corresponds to an incident plane wave and its reflection at the left boundary of the constriction and this corresponds to the solution of the Shrödinger equation at the left most portion of space. The second term of our equation corresponds to the solution at the constriction and it is a combination of all the subband wave functions (left and right current carrying states). Finally the last term which corresponds to the solution at the right most portion of space and it represents transmission through the constriction at $z = d$. Since the energy E in this system is conserved so $\vec{k}_z^2(\vec{k}_x, \vec{k}_y) = 2m^*E/\hbar^2 - \vec{k}_x^2 - \vec{k}_y^2$ and while taking the square root of this quantity, the imaginary part of $k_z(\vec{k}_x, \vec{k}_y)$ is taken to be positive so that the function decays as $z \rightarrow \pm\infty$ in order to get physical solutions. Unknowns in the equation 2.5 should be determined from the boundary conditions at $z = 0$ and $z = d$; continuity of the wave functions gives for $z = 0$

$$\begin{aligned}\Psi_{\vec{K}_i}(x, y, 0) &= e^{ik_{y_0}y} e^{ik_{x_0}x} + \int dk_x dk_y e^{ik_x x} e^{ik_y y} A_{\vec{K}_i}(k_x, k_y) \\ &= \sum_n \left\{ \psi_{n,E}(x, y, 0) \Theta_{n, \vec{K}_i} + \bar{\psi}_{n,E}(x, y, 0) \Delta_{n, \vec{K}_i} \right\}\end{aligned}\quad (2.6)$$

and for $z = d$ we get

$$\begin{aligned}\Psi_{\vec{K}_i}(x, y, d) &= \sum_n \left\{ \psi_{n,E}(x, y, d) \Theta_{n, \vec{K}_i} + \bar{\psi}_{n,E}(x, y, d) \Delta_{n, \vec{K}_i} \right\} \\ &= \int dk_x dk_y e^{ik_z(k_x, k_y)d} e^{ik_x x} e^{ik_y y} B_{\vec{K}_i}(k_x, k_y)\end{aligned}\quad (2.7)$$

Along the x and y direction the wavefunction continuity is guaranteed, since all subband wavefunction solutions in the constriction would satisfy this condition. This continuity of the wave function in the x and y direction guarantees the continuity of its derivative. However in the z direction we calculate the wave function derivative in order to match it at $z = 0$ and $z = d$ and this would give

$$\begin{aligned}\frac{\partial}{\partial z} \Psi_{\vec{K}_i}(x, y, z)|_{z=0} &= ik_{z_0} e^{ik_{y_0}y} e^{ik_{x_0}x} - \int dk_x dk_y ik_z(k_x, k_y) e^{ik_x x} e^{ik_y y} A_{\vec{K}_i}(k_x, k_y) \\ &= \sum_n \left\{ \frac{\partial}{\partial z} \psi_{n,E}(x, y, z)|_{z=0} \Theta_{n, \vec{K}_i} + \bar{\psi}_{n,E}(x, y, z)|_{z=0} \Delta_{n, \vec{K}_i} \right\}\end{aligned}\quad (2.8)$$

this for $z = 0$ and for $z = d$ we get

$$\frac{\partial}{\partial z} \Psi_{\vec{K}_i}(x, y, z)|_{z=d} = \sum_n \left\{ \frac{\partial}{\partial z} \psi_{n,E}(x, y, z)|_{z=d} \Theta_{n, \vec{K}_i} + \bar{\psi}_{n,E}(x, y, z)|_{z=d} \Delta_{n, \vec{K}_i} \right\}$$

$$= \int dk_x dk_y i k_z(k_x, k_y) e^{i k_z(k_x, k_y)d} e^{i k_x x} e^{i k_y y} B_{\vec{k}_i}(k_x, k_y) \quad (2.9)$$

Having expressed the boundary conditions for such a system, the coefficients $A_{\vec{k}_i}(k_x, k_y)$, $B_{\vec{k}_i}(k_x, k_y)$, Θ_{n, \vec{k}_i} and Δ_{n, \vec{k}_i} have to be determined as a function of the incident wave vector \vec{k}_i and this is done by solving equations 2.6, 2.7, 2.8 and 2.9 simultaneously, and $\Psi_{\vec{k}_i}(x, y, z)$ will be determined in all space. Eventhough those coefficients can be determined exactly, the solution is not simple. We need to take the Fourier Transform (FT) of these equations in order to get rid of the x and y dependence in the final expression so that the manipulation of these equations will be easier; to do this we will define the 2D FT of a function $f(x, y)$ as

$$F(q_x, q_y) = \frac{1}{2\pi} \int_{-\infty}^{\infty} dx dy e^{-i q_x x} e^{-i q_y y} f(x, y) \quad (2.10)$$

taking the FT of equation 2.6 and 2.7 we get

$$\begin{aligned} 2\pi \left[\delta(q_x - k_{x_o}) \delta(q_y - k_{y_o}) + A_{\vec{k}_i}(q_x, q_y) \right] = \\ \sum_n \left\{ \Pi_{n,E}(q_x, q_y, 0) \theta_{n, \vec{k}_i} + \bar{\Pi}_{n,E}(q_x, q_y, 0) \Delta_{n, \vec{k}_i} \right\} \\ 2\pi e^{i k_z(q_x, q_y)d} B_{\vec{k}_i}(q_x, q_y) = \\ \sum_n \left\{ \Pi_{n,E}(q_x, q_y, d) \theta_{n, \vec{k}_i} + \bar{\Pi}_{n,E}(q_x, q_y, d) \Delta_{n, \vec{k}_i} \right\} \end{aligned} \quad (2.11)$$

where Π and $\bar{\Pi}$ are used to denote the FT of the subband wave function of ψ and $\bar{\psi}$. Now taking the FT of equations 2.8 and 2.9 we get

$$\begin{aligned} 2\pi \left[i k_{z_o} \delta(q_x - k_{x_o}) \delta(q_y - k_{y_o}) - i k_z(q_x, q_y) A_{\vec{k}_i}(q_x, q_y) \right] = \\ \sum_n \left\{ \Pi'_{n,E}(q_x, q_y, 0) \theta_{n, \vec{k}_i} + \bar{\Pi}'_{n,E}(q_x, q_y, 0) \Delta_{n, \vec{k}_i} \right\} \\ 2\pi i k_z(q_x, q_y) e^{i k_z(q_x, q_y)d} B_{\vec{k}_i}(q_x, q_y) = \\ \sum_n \left\{ \Pi'_{n,E}(q_x, q_y, d) \theta_{n, \vec{k}_i} + \bar{\Pi}'_{n,E}(q_x, q_y, d) \Delta_{n, \vec{k}_i} \right\} \end{aligned} \quad (2.12)$$

where Π' and $\bar{\Pi}'$ are used to denote the subband wave function derivatives of ψ' and $\bar{\psi}'$ along the z -direction. From the previous two equations, elimination of the reflection coefficient $A_{\vec{k}_i}(q_x, q_y)$ gives

$$2\pi [2k_{z_o}] \delta(q_x - k_{x_o}) \delta(q_y - k_{y_o}) =$$

$$\sum_n \left\{ [k_z(q_x, q_y)\Pi_{n,E}(q_x, q_y, 0) - i\Pi'_{n,E}(q_x, q_y, 0)]\theta_{n,\vec{K}_i} + [k_z(q_x, q_y)\bar{\Pi}_{n,E}(q_x, q_y, 0) - i\bar{\Pi}'_{n,E}(q_x, q_y, 0)]\Delta_{n,\vec{K}_i} \right\} \quad (2.13)$$

and the elimination of transmission coefficient $B_{\vec{K}_i}(q_x, q_y)$ gives

$$\sum_n \left\{ [k_z(q_x, q_y)\Pi_{n,E}(q_x, q_y, d) + i\Pi'_{n,E}(q_x, q_y, d)]\theta_{n,\vec{K}_i} + [k_z(q_x, q_y)\bar{\Pi}_{n,E}(q_x, q_y, d) + i\bar{\Pi}'_{n,E}(q_x, q_y, d)]\Delta_{n,\vec{K}_i} \right\} = 0 \quad (2.14)$$

Equation 2.13 and 2.14 have to be solved simultaneously to obtain the coefficients θ_{n,\vec{K}_i} and Δ_{n,\vec{K}_i} where \vec{K}_i is the incident plane wave vector. Here we note that equation 2.13 stands for the transmission of incident plane wave into the subband states at the entrance of constriction ($z = 0$), and equation 2.14 corresponds to the reflection of subband at the end of constriction ($z = d$). Therefore once the solution of Shrödinger equation (equation 2.4) in the constriction is determined and the subband wave functions are known, the problem reduces to calculation of multiple reflections from the edges of the constriction. It is then a simple algebraic problem.

Assuming that these coefficients are determined, and $\Psi_{\vec{K}_i}(x, y, z)$ is calculated throughout the constriction, we will determine the current passing across the constriction in order to find out the conductivity. In order to calculate the current, it is clear that calculating I_{z_o} through any z contact crossing the z -axis at $z = z_o$ would yield the same result, since the current inside the system is conserved. To do this we choose ($z < z_o < d$), so that the final current expression consists of subband wave functions. The current passing through the QPC is related to the occupation of subbands as in the Landauer formula.^{8,16}

The current due to incident waves ψ_α and ψ_β with energy E can be written using the expectation value of the current operator

$$\langle \psi_\alpha | \hat{j} | \psi_\beta \rangle = \frac{\hbar}{2im^*} \int dx dy \left[\psi_\alpha^*(x, y) \psi'_\beta(x, y) - \psi_\alpha^{\prime*}(x, y) \psi_\beta(x, y) \right] \quad \P \quad (2.15)$$

^{\P} Here we note that we are using the sign * in order to denote the effective mass if it is a superscript of the character m , and a complex conjugate for any other variable.

In our system we should take into account all contributions from all incoming states $\Psi_{\vec{K}_i}$. Hence,

$$J(E) = 2e \int \frac{d\vec{K}_i^3}{(2\pi)^3} \langle \Psi_{\vec{K}_i}(x, y, z) | \hat{j} | \Psi_{\vec{K}_i}(x, y, z) \rangle |_{z=z_0} \delta\left(\frac{\hbar^2 |\vec{K}_i|^2}{2m^*} - E\right) \Theta(k_{z_0}) \quad (2.16)$$

Where $J(E)$ corresponds to the electric current due to the states with energy E . Here we have introduced the factor e in order to convert the probability current into the electrical current. The prefactor 2 takes care of spin degeneracy and $1/(2\pi)^3$ is the density of states in the 3D K -space, δ function selects the states which have energy E and the step function Θ selects electrons with positive \vec{k}_{z_0} , so that only electrons entering the channel are taken into account. In order to evaluate $J(E)$ we will initially calculate $\langle \Psi_{\vec{K}_i} | \hat{j} | \Psi_{\vec{K}_i} \rangle$ at an arbitrary point $z = z_0$ in the constriction.

$$\begin{aligned} \langle \Psi_{\vec{K}_i} | \hat{j} | \Psi_{\vec{K}_i} \rangle |_{z=z_0} &= \frac{\hbar}{2im^*} \int dx dy \\ &\sum_{m,n} \left\{ [\psi_{n,E}^* |_{z=z_0} \Theta_{n,\vec{K}_i}^* + \bar{\psi}_{n,E}^* |_{z=z_0} \Delta_{n,\vec{K}_i}^*] [\psi'_{m,E} |_{z=z_0} \Theta_{m,\vec{K}_i} + \bar{\psi}'_{m,E} |_{z=z_0} \Delta_{m,\vec{K}_i}] \right. \\ &\left. - [\psi_{n,E}^* |_{z=z_0} \Theta_{n,\vec{K}_i}^* + \bar{\psi}_{n,E}^* |_{z=z_0} \Delta_{n,\vec{K}_i}^*] [\psi_{m,E} |_{z=z_0} \Theta_{m,\vec{K}_i} + \bar{\psi}_{m,E} |_{z=z_0} \Delta_{m,\vec{K}_i}] \right\} \end{aligned} \quad (2.17)$$

In this equation, for clarity we have dropped the (x, y, z) factor which is in the front of the subband wave functions; further manipulation of this equation yields

$$\begin{aligned} \langle \Psi_{\vec{K}_i} | \hat{j} | \Psi_{\vec{K}_i} \rangle |_{z=z_0} &= \frac{\hbar}{m^*} \int dx dy \sum_{m,n} \Im m \left\{ \Theta_{n,\vec{K}_i}^* \psi_{n,E}^* |_{z=z_0} \psi'_{m,E} |_{z=z_0} \Theta_{m,\vec{K}_i} \right. \\ &+ \Delta_{n,\vec{K}_i}^* \bar{\psi}_{n,E}^* |_{z=z_0} \bar{\psi}'_{m,E} |_{z=z_0} \Delta_{m,\vec{K}_i} + \Theta_{n,\vec{K}_i}^* \psi_{n,E}^* |_{z=z_0} \bar{\psi}'_{m,E} |_{z=z_0} \Delta_{m,\vec{K}_i} \\ &\left. + \Delta_{n,\vec{K}_i}^* \bar{\psi}_{n,E}^* |_{z=z_0} \psi_{m,E} |_{z=z_0} \Theta_{m,\vec{K}_i} \right\} \end{aligned} \quad (2.18)$$

Finally we obtain

$$J(E) = \frac{e}{\pi \hbar} \frac{1}{2\pi} \oint_{k_{x_0}^2 + k_{y_0}^2 < K_E^2} \frac{dk_{x_0} dk_{y_0}}{k_{z_0}} \sum_{m,n} \Im m \left\{ \Theta_{n,\vec{K}_i}^* \left[\int dx dy \psi_{n,E}^* |_{z=z_0} \psi'_{m,E} |_{z=z_0} \right] \Theta_{m,\vec{K}_i} \right\}$$

$$\begin{aligned}
 & +\Delta_{n,K_i}^* \left[\int dx dy [\bar{\psi}_{n,E}^*|_{z=z_o} \bar{\psi}'_{m,E}|_{z=z_o}] \Delta_{m,K_i} \right. \\
 & +\Theta_{n,K_i}^* \left[\int dx dy \psi_{n,E}^*|_{z=z_o} \bar{\psi}'_{n,E}|_{z=z_o} \right] \Delta_{m,K_i} \\
 & \left. +\Delta_{n,K_i}^* \left[\int dx dy [\bar{\psi}_{n,E}^*|_{z=z_o} \psi'_{m,E}|_{z=z_o}] \Theta_{m,K_i} \right] \right\} \quad (2.19)
 \end{aligned}$$

Here we have introduced a new variable $K_E^2 = E 2m^*/\hbar^2$, and the \oint corresponds to the 2D integration in the k -space such that $k_{x_o}^2 + k_{y_o}^2 < K_E^2$ with the constraint $k_{x_o}^2 + k_{y_o}^2 + k_{z_o}^2 = K_E^2$ has to be satisfied while evaluating the previous integration. Now we will assume that our constriction is connected to two jellium electrodes at $z = \pm\infty$ and the electro-chemical potentials of these two reservoirs are kept constant so that there is an infinitesimal difference $\Delta\mu = \mu_L - \mu_R > 0$ between the electro-chemical potential of the left hand side and the right hand side of the reservoirs. In this circuit current would flow from the left reservoir to the right one and vice versa and in experiment we would measure only the effective one. To measure the current due to one electrode, we should integrate $J(E)$ factored by $D(E)$, which is the electron occupancy with energy E , over all the energy range. In our calculation we will take $D(E) = f_{FD}(E)$ which is the Fermi-Dirac distribution at $T = 0K$ so that it corresponds to step function; therefore the current flowing through the circuit is

$$\begin{aligned}
 I &= \int_0^{\mu_L} J(E) dE - \int_0^{\mu_R} J(E) dE \\
 &= \int_{\mu_L}^{\mu_R} J(E) dE = (\mu_L - \mu_R) J(\mu_R) \quad (\text{where } (\mu_L - \mu_R) \rightarrow 0) \\
 &= \Delta\mu J(E_F) = eV J(E_F) \quad (\mu_R = E_F, \text{ Fermi energy}) \quad (2.20)
 \end{aligned}$$

The conductance is

$$G = \frac{I}{V} = eJ(E_F) \quad (2.21)$$

By determining $J(E)$ from equation 2.19, we obtain directly the conductance in the constriction after multiplying by e . In the next section, we will solve this problem for a uniform constriction, followed by an approximate solution for a more general potential type in section 2.4.

2.2 Cylindrical Infinite Well Confinement

2.2.1 Formalism

In this section we will assume that the confining potential is independent from z . As a result $\phi_m(z) = 0$ and $V_c(x, y, z) = V_c(x, y)$. Furthermore we assume that this potential is only radial. We first treat the infinite wall cylindrical confinement potential in this section. Then we consider parabolic one. Eventhough these profiles oversimplify the real potential, we believe that some insight of the problem could still be grasped. Our potential confinement would have the form

$$V(\vec{r}) = \theta(z)\Theta(d - z)V(\rho) \quad (2.22)$$

$$\text{where } V(\rho) = \begin{cases} 0 & \rho < w \\ \infty & \text{otherwise} \end{cases} \quad (2.23)$$

Where θ , ϕ and z describe cylindrical coordinate system. This describes an infinite cylindrical wall potential with uniform crosssection, in the regions $0 < z < d$ and 0 otherwise. Due to ρ dependence of the potential, we will write Shrödinger equation 2.4 in cylindrical coordinate system and it becomes

$$\left\{ \left[-\frac{\hbar^2}{2m^*} \frac{\partial^2}{\partial z^2} \right] + \left[-\frac{\hbar^2}{2m} \nabla_{\parallel}^2 + V_c(\rho) \right] \right\} \psi_{n,E}(\rho, \phi, z) = E \psi_{n,E}(\rho, \phi, z) \quad (2.24)$$

where

$$\nabla_{\parallel}^2 = \frac{1}{\rho} \frac{\partial}{\partial \rho} \rho \frac{\partial}{\partial \rho} + \frac{1}{\rho^2} \frac{\partial^2}{\partial \phi^2} \quad (2.25)$$

in cylindrical coordinate system; this equation is separable and we can write

$$\psi_{n,E}(\rho, \phi, z) = e^{i\gamma_n z} \Phi_n(\rho, \phi) \quad (2.26)$$

where the lateral wave function satisfies the differential equation

$$\left[-\frac{\hbar^2}{2m} \nabla_{\parallel}^2 + V_c(\rho) \right] \Phi_n(\rho, \phi) = \epsilon_n \Phi_n(\rho, \phi) \quad (2.27)$$

with subband energy ϵ_n and propagation vector along the z -axis γ_n satisfying

$$\gamma_n = \sqrt{\frac{2m^*}{\hbar} (E - \epsilon_n)} \quad (2.28)$$

where the root with positive imaginary value is taken.

Since the potential in equation 2.27, has only ρ dependence, we can separate our equation into radial and rotational parts and we can make the following transformation: $\Phi_n(\rho, \phi) \rightarrow \Phi_{nl}(\rho, \phi) = R_{nl}(\rho)e^{il\phi}$ where the radial part R_{nl} satisfies

$$\left\{ -\frac{\hbar^2}{2m} \frac{1}{\rho} \frac{d}{d\rho} \rho \frac{d}{d\rho} + \frac{\hbar^2 l^2}{2m\rho^2} \right\} R_{nl}(\rho) = \epsilon_{nl} R_{nl}(\rho) \quad (2.29)$$

with boundary condition $R_{nl}(w) = 0$

Manipulating this equation with transformation $\rho = au$ we get the following form

$$\left\{ u \frac{d}{du} u \frac{d}{du} + (u^2 - l^2) \right\} R_{nl}(u) = 0 \quad (2.30)$$

where $\frac{2ma^2}{\hbar^2} \epsilon_{nl} = 1$
and $R_{nl}\left(\frac{w}{a}\right) = 0$

This represents Bessel's equation of the first kind and its solution $J_l(u)$ is straight forward, however, the vanishing of the function at the boundary yields to only some possible eigenstate solutions

$$R_{nl}(\rho) = A_{nl} J_l\left(u_{nl} \frac{\rho}{w}\right) \quad (2.31)$$

and $\epsilon_{nl} = \frac{\hbar^2}{2mw^2} u_{nl}^2$

Hence the lateral wave functions have the form

$$\Phi_{nl}(\rho, \phi) = A_{nl} J_l\left(u_{nl} \frac{\rho}{w}\right) e^{il\phi} \quad (2.32)$$

where l is the order of the Bessel function and u_{nl} its n^{th} zero, while the term A_{nl} corresponds to the normalization constant solved through the equation

$$\int_0^w \rho d\rho \int_0^{2\pi} d\phi \Phi_{nl}(\rho, \phi) \Phi_{n'l'}^*(\rho, \phi) = \delta_{nn'} \delta_{ll'} \quad (2.33)$$

By solving this equation to find A_{nl} , we get the final form of the lateral wave function as

$$\Phi_{nl}(\rho, \phi) = \frac{1}{\sqrt{\pi} w} \frac{J_l\left(u_{nl} \frac{\rho}{w}\right)}{J_{l+1}(u_{nl})} e^{il\phi} \quad (2.34)$$

From equation 2.28 the longitudinal wave vector have the form

$$\begin{aligned} \gamma_{nl} &= \sqrt{-\frac{2m}{\hbar^2}\epsilon_{nl} + k_F^2} = k_F \sqrt{-\left(\frac{u_{nl}}{k_F w}\right)^2 + 1} \\ \text{thus} \quad \frac{\gamma_{nl}}{k_F} &= \sqrt{1 - \frac{(u_{nl}/2\pi)^2}{(w/\lambda_F)^2}} \end{aligned} \quad (2.35)$$

In the previous section we have shown how the solution of such a system is manipulated by taking the FT in the x and y directions, so now we will calculate this in cylindrical coordinate system using

$$F(\vec{\kappa}) = \frac{1}{2\pi} \int e^{-i\vec{\kappa}\cdot\vec{\rho}} f(\vec{\rho}) d\vec{\rho} \quad (2.36)$$

and

$$\begin{aligned} \Phi_{nl}(\kappa, \theta_\kappa) &= \frac{1}{2\pi} \int_0^w \int_0^{2\pi} \rho d\rho d\phi e^{i\kappa\rho \cos(\phi-\theta_\kappa)} A_{nl} J_l\left(u_{nl} \frac{\rho}{w}\right) e^{il\phi} \\ &= \frac{1}{\sqrt{\pi}} \frac{w}{u_{nl}} e^{il\theta_\kappa} i^l \frac{1}{1 - \left(\frac{\kappa w}{u_{nl}}\right)^2} J_l(\kappa w) \end{aligned} \quad (2.37)$$

We note here that in this section we are using $\vec{\kappa} = (\kappa, \theta_\kappa)$ instead of (q_x, q_y) as the FT basis. We will write again equations 2.13 and 2.14 which now have much simpler form

$$2\pi 2k_{z_o} \delta(\vec{\kappa} - \vec{\kappa}_o) = \sum_{nl} \left\{ [k_z(\kappa) + \gamma_{nl}] \Theta_{nl, \vec{k}_i} + [k_z(\kappa) - \gamma_{nl}] \Delta_{nl, \vec{k}_i} \right\} \Phi_{nl}(\vec{\kappa}) \quad (2.38)$$

and

$$\sum_{nl} \left\{ [k_z(\vec{\kappa}) - \gamma_{nl}] e^{i\gamma_{nl}d} \Theta_{nl, \vec{k}_i} + [k_z(\kappa) + \gamma_{nl}] e^{-i\gamma_{nl}d} \Delta_{nl, \vec{k}_i} \right\} \Phi_{nl}(\vec{\kappa}) = 0 \quad (2.39)$$

In order to solve such a system we will multiply every equation (2.38 and 2.39) by $\Phi_{n'l'}^*(\vec{\kappa})$ and integrate over all $\vec{\kappa}$ values, while using the orthogonality relation of the lateral wave functions and thus its FT. The resulting equations are

$$2\pi i 2k_{z_o} \Phi_{n'l'}^*(\vec{\kappa}_o) = \sum_{nl} [i \{ K_{n'l',nl} + \gamma_{nl} \delta_{nn'} \delta_{ll'} \} \Theta_{nl} + i \{ K_{n'l',nl} - \gamma_{nl} \delta_{nn'} \delta_{ll'} \} \Delta_{nl}] \quad (2.40)$$

and

$$\sum_{nl} \left[i \{ K_{n'l';nl} - \gamma_{nl} \delta_{nn'} \delta_{ll'} \} e^{i\gamma_{nl}d} \Theta_{nl} + i \{ K_{n'l';nl} + \gamma_{nl} \delta_{nn'} \delta_{ll'} \} e^{-i\gamma_{nl}d} \Delta_{nl} \right] = 0 \quad (2.41)$$

Here $\delta_{nn'}$ is the Kronecker delta, and the matrix element $K_{n'l';nl}$ is defined through the relation

$$K_{n'l';nl} = \int d\vec{k} \Phi_{n'l',nl}^*(\vec{k}) k_z(\vec{k}) \Phi_{n'l',nl}(\vec{k}) \quad (2.42)$$

Now we can rewrite equations 2.40 and 2.41 in a matrix form so that we can drop off our summation terms and we would obtain

$$2\pi i 2k_{z_o} \tilde{\Phi}^\dagger(\vec{k}_o) = i(\tilde{K} + \tilde{\Gamma})\tilde{\Theta} + i(\tilde{K} - \tilde{\Gamma})\tilde{\Delta} \quad (2.43)$$

and

$$i(\tilde{K} - \tilde{\Gamma})e^{i\tilde{\Gamma}d}\tilde{\Theta} + i(\tilde{K} + \tilde{\Gamma})e^{-i\tilde{\Gamma}d}\tilde{\Delta} = 0 \quad (2.44)$$

Here $\tilde{\Theta}$ and $\tilde{\Delta}$ correspond to the column vectors of the coefficients of the subband wave functions with right and left going probability currents, respectively. $\tilde{\Phi}$ is the row vector of the transverse FT of the lateral wave functions. $\tilde{\Gamma}$ is a diagonal matrix of propagation constant vectors corresponding to every eigen state, and \tilde{K} is the longitudinal momentum matrix.

Now equations 2.43 and 2.44 correspond to the boundary conditions at $z = 0$ and $z = d$ respectively and they can be easily solved to find out the subband coefficients

$$\tilde{\Delta} = e^{i\tilde{\Gamma}d}(\tilde{K} + \tilde{\Gamma})^{-1}(\tilde{K} - \tilde{\Gamma})e^{i\tilde{\Gamma}d}\tilde{\Theta} \quad (2.45)$$

$$\tilde{\Theta} = 2\pi \left\{ \tilde{1} - \left[(\tilde{K} + \tilde{\Gamma})^{-1}(\tilde{K} - \tilde{\Gamma})e^{i\tilde{\Gamma}d} \right]^2 \right\}^{-1} 2k_{z_o}(\tilde{K} + \tilde{\Gamma})^{-1}\tilde{\Phi}^\dagger(\vec{k}_o) \quad (2.46)$$

In order to find current $J(E_F)$ we refer back to equations 2.18 and 2.19 and we would get

$$\begin{aligned} \langle \Psi | j | \Psi \rangle &= \frac{\hbar}{m^*} \Im m \left\{ i\tilde{\Theta}^\dagger \tilde{\Gamma} \tilde{\Theta} - i\tilde{\Delta}^\dagger \tilde{\Gamma} \tilde{\Delta} + i\tilde{\Delta}^\dagger \tilde{\Gamma} \tilde{\Theta} - i\tilde{\Theta}^\dagger \tilde{\Gamma} \tilde{\Delta} \right\} \\ &= \frac{\hbar}{m^*} \left\{ [\tilde{\Theta}^\dagger \tilde{\Gamma}_R \tilde{\Theta} - \tilde{\Delta}^\dagger \tilde{\Gamma}_R \tilde{\Delta}] + 2[\tilde{\Theta}^\dagger \tilde{\Gamma}_I \tilde{\Delta}] \right\} \end{aligned} \quad (2.47)$$

where Γ_R and Γ_I are the real and imaginary matrices of the matrix Γ , respectively. From these results, equation 2.19 would give us much simpler form by replacing the cartesian coordinate system with cylindrical one and by using the fact that equations are independent of θ_κ . Thus

$$J(E_F) = \frac{2e}{h} \frac{1}{2\pi} \int_0^{K_F} \frac{\kappa d\kappa}{k_z(\kappa)} \left\{ [\tilde{\Theta}^\dagger \tilde{\Gamma}_R \tilde{\Theta} - \tilde{\Delta}^\dagger \tilde{\Gamma}_R \tilde{\Delta}] + 2\Im m[\tilde{\Theta}^\dagger \tilde{\Gamma}_I \tilde{\Delta}] \right\} \quad (2.48)$$

To further simplify we introduce the following matrices

$$\tilde{\Pi} = 2 \left[\tilde{I} - \tilde{r} e^{i\tilde{\Gamma}d} \tilde{r} e^{i\tilde{\Gamma}d} \right]^{-1} (\tilde{K} + \tilde{\Gamma})^{-1} \quad (2.49)$$

$$\tilde{\Lambda} = e^{i\tilde{\Gamma}d} \tilde{r} e^{i\tilde{\Gamma}d} \tilde{\Pi} \quad (2.50)$$

$$\tilde{r} = (\tilde{K} + \tilde{\Gamma})^{-1} (\tilde{\Gamma} - \tilde{K}) \quad (2.51)$$

As a result, the conductance becomes

$$G = \frac{2e^2}{h} 2\pi \int_0^{K_F} \frac{\kappa d\kappa}{k_z(\kappa)} k_z^2(\kappa) \left\{ \tilde{\Phi}(\kappa) [\tilde{\Pi}^\dagger \tilde{\Gamma}_R \tilde{\Pi} - \tilde{\Lambda}^\dagger \tilde{\Gamma}_R \tilde{\Lambda}] \tilde{\Phi}^\dagger(\kappa) + 2\Im m \tilde{\Phi}(\kappa) [\tilde{\Pi}^\dagger \tilde{\Gamma}_I \tilde{\Lambda}] \tilde{\Phi}^\dagger(\kappa) \right\} \quad (2.52)$$

In this equation only k_{z_0} and $\tilde{\Phi}$ are function of κ . Since $k_z(\kappa)$ is real for $|\kappa| < K_F$; one gets, by using equation 2.42,

$$\Re e \tilde{K} = 2\pi \int_0^{K_F} \kappa d\kappa \tilde{\Phi}^\dagger(\kappa) k_z(\kappa) \tilde{\Phi}(\kappa) \quad (2.53)$$

Finally the conductance formula reduces to the form

$$G = \frac{2e^2}{h} tr \left\{ \left[\tilde{\Pi}^\dagger \tilde{\Gamma}_R \tilde{\Pi} - \tilde{\Lambda}^\dagger \tilde{\Gamma}_R \tilde{\Lambda} + 2\Im m(\tilde{\Pi}^\dagger \tilde{\Gamma}_I \tilde{\Lambda}) \right] \Re e \left[\tilde{K} \right] \right\} \quad (2.54)$$

In this equation there are 3 terms contributing to the conductivity; the first and the second term correspond to right and left going waves in the constriction, respectively. Resonance effect may appear in the system due to their relative phase difference. The third term, corresponds to evanescent states[¶] in the constriction.¹³ For finite length constrictions, where tunneling phenomenon becomes important, this last term becomes important since it yields deviations from sharp steps structure.

[¶]Assuming perfect conductivity in the constriction; i.e, as $d \rightarrow \infty$, such states (with $\epsilon_{nl} > E_F$) do not contribute to conductivity

Before introducing our results, we would like to bring the following issue to the reader attention: Since we are measuring conductivity for a ballistic system (no scattering is occurring), shouldn't we get $G \rightarrow \infty$?

In fact this question has been addressed previously, while calculating the conductivity of *2DEG QPC*. Imry³⁵ has showed that the finite resistance obtained in such formulae was the contact resistance and did not correspond to the constriction resistance which has to be zero. This type of resistance measurement is known as two probe measurement and it has been thought that the resistance of a perfect conductor vanishes for *four*-probe measurement, where one uses different probes for the current and voltage measurements which are very weakly coupled to the device. In experimental set up, however, the lithographic shape of the current and voltage probes are the same in the *two*-probe as well as the *four*-probe measurements. For this reason it becomes impossible to assume weak coupling for the voltage probes. In fact Büttiker^{36,37} has considered the coherent device consisting of the probes in addition to the loops or wire and calculated the scattering matrix for this device, where all probes are assumed to be connected to reservoirs at equilibrium. He has found that the resistance vanishes only for very weak coupling (*four*-probe measurement) which does not correspond to the experimental conditions. As a result we have used *two*-probe measurement to calculate the conductivity in our theoretical study.

2.2.2 Results

In equation 2.54 we have obtained the final result of the conductivity for a perfectly cylindrical potential, by the integration over all the incident wave vectors in equation 2.52. The result is expressed only in terms of matrices. However, here we would like to mention an important difference between our results and experiments in which conductivity is measured. In the latter, G is measured as a function of V_p (piezo voltage) or the neck length, whereas in the former, it is calculated as a function of the electron density (or equivalently λ_F) and the area of the constriction A . Here we note that this main difference in conductivity

measurement is due to the fact that in the theoretical studies, energy bands below the Fermi level (which defines our contact area) are the criteria for the conductivity; however, experimentally, it is not possible to measure the contact area at the constriction. On the other hand, there were attempts to estimate the confining potential profile (which would give the contact area) as a function of pulling using simulations with molecular dynamics,³⁸ but these profiles are not universal because they are obtained by empirical potential, and depend on initial structure configuration and stretch speed. It is, therefore, difficult to find out the correct potential profile confinement. Nevertheless, our SCF calculations as well as others',^{13,34} have shown that parabolic potential confinement works well for one atom contact and infinite wall cylindrical potential parameterization is good for many atom point contact and this has motivated us to use them.

As shown in the previous section, we have to calculate the propagation matrix $\tilde{\Gamma}$ given by $\Gamma_{nl,n'l'} = \gamma_{nl}\delta_{nn'}\delta ll'$ and we should evaluate numerically the longitudinal matrix \tilde{K} given in equation 2.42 with the wave functions described by equation 2.37. An important point that is worth mentioning is that the off-diagonal elements of \tilde{K} are very small compared to the diagonal elements. For the infinite wall confinement, they deviate from zero and they become appreciable only when the energy of the subband dips below the Fermi level. Thus $\tilde{\Gamma}$ and \tilde{K} can be represented by finite dimensions, since in our calculations, we are interested at most upto the 5th energy subband. As a result, contributions from higher energy subbands would be small and we have noticed that 12x12 matrices give results with convergence less than 2%, and in all our calculations we have used 20 subbands to get better convergence.

Initially, we will investigate the case of a semiinfinite constriction. In such a system contributions from the left going and evanescent states should be eliminated and, hence equation 2.54 becomes

$$G = \frac{2e^2}{h} tr \left\{ 4([\tilde{K} + \tilde{\Gamma}]^{-1})^\dagger \tilde{\Gamma}_R [\tilde{K} + \tilde{\Gamma}]^{-1} \Re(\tilde{K}) \right\} \quad (2.55)$$

In Figure 2.1, we show the results for a perfect semiinfinite constriction, in which approximate quantization of conductance is apparent. This point is quite

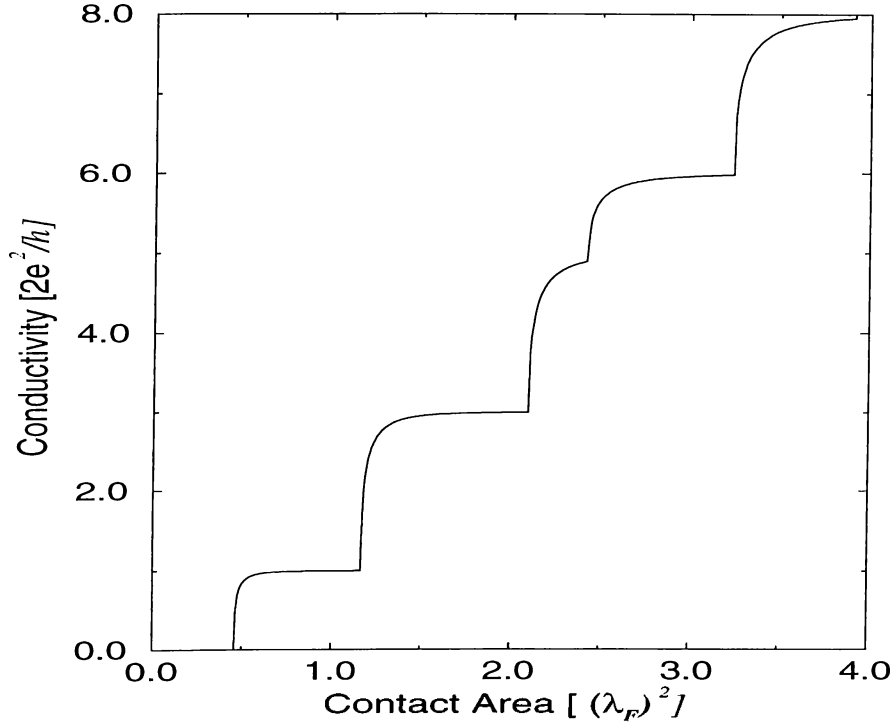


Figure 2.1: Conductance vs contact area due to transmission into semiinfinite uniform constriction with cylindrical potential confinement

understandable, since $K_{nn} \simeq \gamma_{nn}$, so that the trace in equation 2.55 approaches to N_p . Now if we consider incidence from the constriction, the reflection amplitudes are given by equation 2.51. Here one can directly use conventional Landauer's formula⁸ in the channel and we get

$$G_L = \frac{2e^2}{h} \left\{ N_p - \text{tr}[\tilde{r}^\dagger \tilde{r}] \right\} \quad (2.56)$$

where the first term is just the number of occupied subbands N_p in the constriction and gives the incident waves. The second term is the contribution of the reflected waves. Here we note that $G = G_L$ as a result of time-reversal symmetry.

After examining the the semiinfinite constriction case, we will focus on the finite length channels, here we will solve equation 2.54 completely to find the conductivity. The results of our calculations for finite length constriction are illustrated in Figure 2.2.

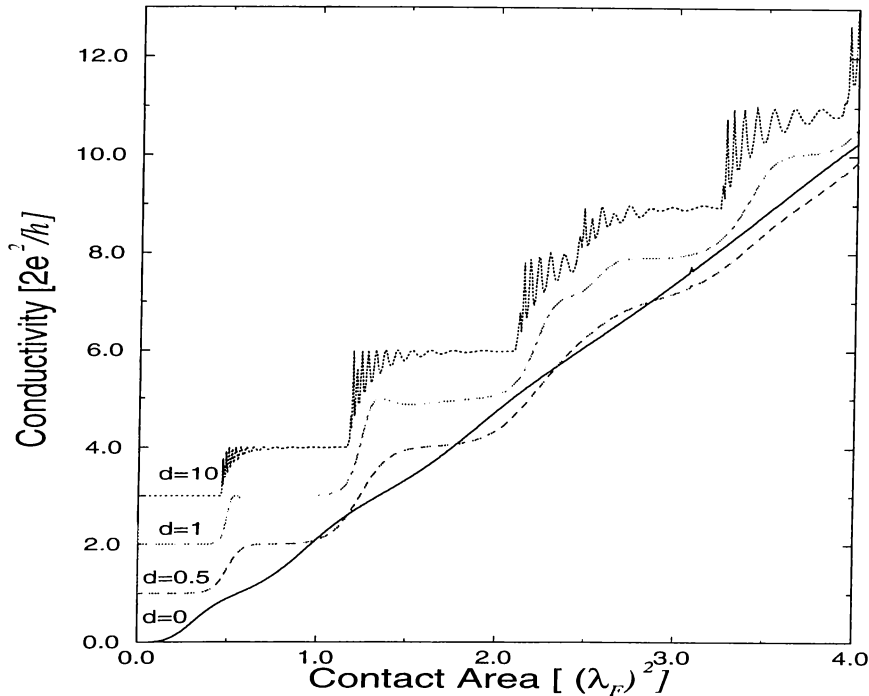


Figure 2.2: Conductance versus contact area due to transmission into a finite length uniform constriction with cylindrical potential confinement. The length of the constriction d is in units of λ_F . The graphs have been shifted for clarity.

The zero-length *QPC* was studied earlier.⁶ Comparing the result obtained by using this formalism with Sharvin's calculations,⁶ we observe a great resemblance between them. The sharp quantum steps have disappeared and there is a linear relation between the conductivity and the contact area as predicted previously by Sharvin. The washing of the quantum steps is not surprising, since as $d \rightarrow 0$ the probability of tunneling becomes appreciable and this phenomenon dominates the conductivity. However, we can see in Figure 2.2 some deviations from Sharvin's calculations; it is obvious that the "straight line" does not pass through the origin and it exhibits some weak oscillations. The shift of the "straight line" towards a larger contact area (A) value can be understood in terms of Heisenberg uncertainty relation. $\Delta\rho\Delta p_\rho \geq \hbar$, therefore as $\Delta\rho \rightarrow 0$ the transverse momentum $\Delta p_\rho \rightarrow +\infty$. Since the largest possible transverse momentum is $\hbar k_F$, if $\rho k_F \leq 1$ (or $A[\lambda_F^2] \leq 0.08$) transport is suppressed to yield zero conductance as one notices

in our graph. The weak oscillations, on the other hand, may be thought as being the precursors to quantized conductance. For $\epsilon_{nl} > E_F$ the transport is via tunneling and the conductance increases exponentially; when this subband dips in the Fermi level, the nature of transport changes to ballistic transport, and the maximum conductance for the subband is limited by the quantum of conductance ($m2e^2/h$ where m is the degeneracy of the state). Therefore the conductance due to this single subband saturates leading to the formation of weak shoulder like features as it is shown in our graph.

As the length of the constriction increases, tunneling contribution decreases and step structure of the conductivity starts to appear. The aforementioned weak oscillations superposed on the classical Sharvin conductance, evolve to form quantized plateaus for $d \geq \lambda_F/2$. This quantization phenomenon gets better with increasing d and they occur at multiples of $2e^2/h$ with a step jump of *one* or *two* quantum steps corresponding to the degeneracy of the wave function in the cylindrical coordinate system. It should be noted that these quantized steps do not represent the real experimental results represented in Figures 1.5, 1.6 and 1.7. In the experiments the plateaus are sharp and they do not display the same degeneracy, while in the theoretical calculations the conductance displays oscillations below the quantized values which increase for larger constriction lengths (d) and subbands with smaller energy eigenstates. These oscillations are due to resonances caused by the interface of right and left going wavefunctions in the constriction. To analyze these resonances, we examine equation 2.50. The matrix $exp[i\tilde{\Gamma}d]$ consists of pure phases for occupied subbands and varying the contact area (A) (i.e varying $\tilde{\Gamma}$), these phases change as well, and this yield an interface between the first and second term in the brackets in equation 2.54. After understanding the origin of these resonances, we won't study this further. The subject of resonance was taken into consideration throughly in previous studies.^{9,13} Next we will generalize our formalism to a much more complicated potential profile in order to represent the experimental confinement better.

2.3 Parabolic Potential Confinement

We have also solved our problem for a parabolic potential type. We have taken the potential form as

$$V(x, y, z) = \frac{1}{2}mw^2(x^2 + y^2) \quad (2.57)$$

This would give a separable solution in the form of $\phi(x)\phi(y)$, where ϕ is Hermite polynomial. The Fourier transform of these functions would also yield to Hermite polynomials. But unfortunately, the \tilde{K} matrix is not as simple as in the previous case (cylindrical infinite well confinement). Therefore, we have followed the same procedure described in the previous section, but evaluated our quantities numerically. Here we note that we have defined our length scale $w_o = \sqrt{\hbar/mw}$ while calculating the contact area. We show our results in Figure 2.3. In our plot, the step structure is resolved with a jump step of order $1G_o$, $2G_o$ and $3G_o$. This is due to the degeneracy for $2D$ parabolic potential. We note

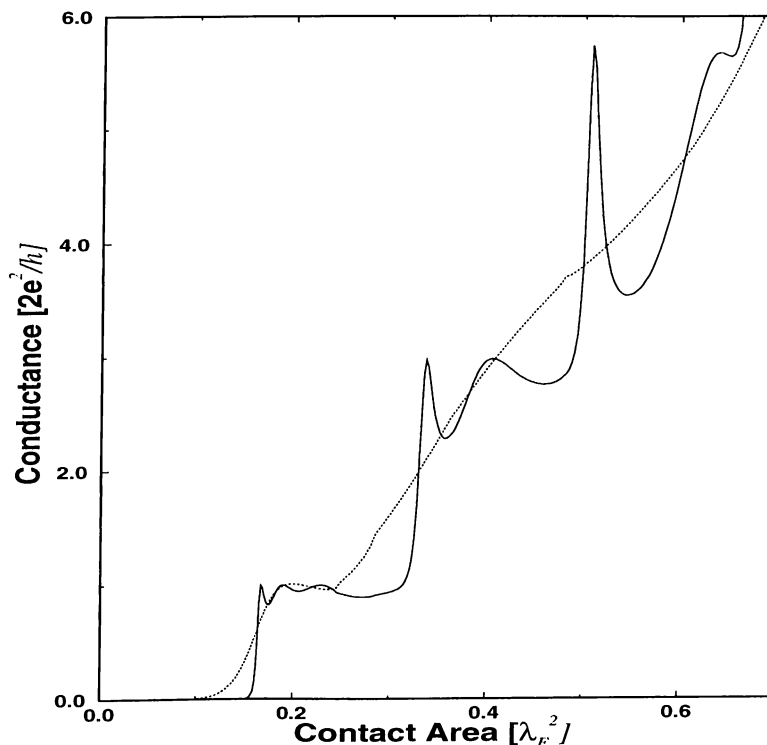


Figure 2.3: Conductance G versus crosssection A of the wire, using parabolic potential form. Continuous and dotted lines are for $\Delta l = \Lambda_f$ and $\Delta l = \Lambda_f/2$, respectively

that the step structure is not well resolved as in the case for the infinite well confinement. For $d = \lambda_F/2$, only the first step is resolved. For $G > G_o$, the plot resembles the Sharvin's conductance. This is due to tunneling phenomenon which becomes pronounced for finite well potential. For $d = \lambda_F$, oscillations start to appear on the plateau of conductance. Comparison of these results with the infinite well confinement, shows that the latter gives much better results compared with experiments. Therefore, while generalizing our method to a more realistic potential, we will consider only infinite cylindrical wall.

2.4 Nonuniform constriction

2.4.1 Transfer Matrix Method

Eventhough in the previous section we could grasp the causes of quantization for conductivity, we could not get features that match with the experimental results. Therefore, we have to generalize our formalism to a much more realistic confinement, which includes the geometrical effects playing crucial roles in the quantization of conductance. In order to obtain conductance versus A curve for a realistic potential, we use the transfer matrix method. The underlying idea for the transfer matrix method is to divide the space into a number of small segments. Using the usual boundary matching technique (applied previously) at the interfaces between segments, the approximate solution is obtained for this piecewise constant potential profile. Increasing the number of segments until the convergence of the solution is obtained, the deviation between the exact and approximate solutions can be made negligibly small.

Following the same reasoning, in our problem, we divide the nonuniform constriction into a large number of segments. In every segment $\phi_m(z)$ and $V_c(x, y, z)$ are assumed to be constant, $\phi_m(z_i)$ and $V_c(x, y, z_i)$ at the i^{th} segment. Thus, the solution for the subband wave function in this segment is the same as that of a uniform constriction with confining potential $V_c(x, y, z_i)$ and the zero of energy is shifted by $\phi_m(z_i)$. Now we will divide the constriction into N segments

and we would call our end points z_o (at $z=0$) and z_N (at $z=d$); the subband wave functions in the interval $z_{i-1} < z < z_i$ is

$$\Psi_{\vec{k}_i}(x, y, z) = \sum_{nl} \left\{ \Theta_{nl}^{(i)} e^{i\gamma_{nl}(z_i)(z-z_{i-1})} + \Delta_{nl}^{(i)} e^{-i\gamma_{nl}(z_i)(z-z_{i-1})} \right\} \psi_{nl}(x, y, z_i) \quad (2.58)$$

where the lateral wave function $\psi_{nl}(x, y, z_i)$ in the i^{th} segment is defined by the equation

$$\left[-\frac{\hbar^2}{2m^*} \nabla_{\parallel}^2 + V_c(x, y, z_i) + \phi_m(z_i) \right] \psi_{nl}(x, y, z_i) = \epsilon_{nl}(z_i) \psi_{nl}(x, y, z_i) \quad (2.59)$$

with subband energy $\epsilon_{nl}(z_i)$ and constant propagation vector

$$\gamma_{nl}(z_i) = \sqrt{\frac{2m^*}{\hbar^2} [E - \epsilon_{nl}(z_i)]} = \gamma_{nl}^{(i)} \quad (2.60)$$

which is a function of segment index. Next, we have to find out the transfer matrix along the constriction. This is done by matching the wave function and its derivative at the interfaces between the segments. To do this, we consider the interface at $z = z_i$ ($0 < i < N$) and we write our equation in intervals $z_{i-1} < z < z_i$ and $z_i < z < z_{i+1}$ in the same form as equation 2.58 to get

$$\begin{aligned} \Psi_{\vec{k}_i}(x, y, z_i) &= \sum_{nl} \left\{ \Theta_{nl}^{(i)} e^{i\gamma_{nl}^{(i)} \Delta z_i} + \Delta_{nl}^{(i)} e^{-i\gamma_{nl}^{(i)} \Delta z_i} \right\} \psi_{nl}^{(i)} \\ &= \sum_{nl} \left\{ \Theta_{nl}^{(i+1)} + \Delta_{nl}^{(i+1)} \right\} \psi_{nl}^{(i+1)} \end{aligned} \quad (2.61)$$

and its derivative along the z axis gives

$$\begin{aligned} \frac{\partial \Psi_{\vec{k}_i}(x, y, z)}{\partial z} \Big|_{z=z_i} &= \sum_{nl} i\gamma_{nl}^{(i)} \left\{ \Theta_{nl}^{(i)} e^{i\gamma_{nl}^{(i)} \Delta z_i} - \Delta_{nl}^{(i)} e^{-i\gamma_{nl}^{(i)} \Delta z_i} \right\} \psi_{nl}^{(i)} \\ &= \sum_{nl} i\gamma_{nl}^{(i+1)} \left\{ \Theta_{nl}^{(i+1)} - \Delta_{nl}^{(i+1)} \right\} \psi_{nl}^{(i+1)} \end{aligned} \quad (2.62)$$

where $\Delta z_i = z_i - z_{i-1}$ is the i^{th} segment length and $\psi_{nl}^{(i)}$ corresponds to $\psi_{nl}(x, y, z_i)$. The previous two equations yield to

$$\sum_{nl} \left\{ \Theta_{nl}^{(i)} e^{i\gamma_{nl}^{(i)} \Delta z_i} + \Delta_{nl}^{(i)} e^{-i\gamma_{nl}^{(i)} \Delta z_i} \right\} \psi_{nl}^{(i)} = \sum_{nl} \left\{ \Theta_{nl}^{(i+1)} + \Delta_{nl}^{(i+1)} \right\} \psi_{nl}^{(i+1)} \quad (2.63)$$

and

$$\sum_{nl} i\gamma_{nl}^{(i)} \left\{ \Theta_{nl}^{(i)} e^{i\gamma_{nl}^{(i)} \Delta z_i} - \Delta_{nl}^{(i)} e^{-i\gamma_{nl}^{(i)} \Delta z_i} \right\} \psi_{nl}^{(i)} = \sum_{nl} i\gamma_{nl}^{(i+1)} \left\{ \Theta_{nl}^{(i+1)} - \Delta_{nl}^{(i+1)} \right\} \psi_{nl}^{(i+1)} \quad (2.64)$$

Multiplying equations 2.63 and 2.64 by $\psi_{nl}^{(i)\dagger}$ and integrating over all x and y we get

$$\Theta_{nl}^{(i)} e^{i\gamma_{nl}^{(i)} \Delta z_i} + \Delta_{nl}^{(i)} e^{-i\gamma_{nl}^{(i)} \Delta z_i} = \sum_{n'l'} \left\{ \Theta_{n'l'}^{(i+1)} + \Delta_{n'l'}^{(i+1)} \right\} S_{nl,n'l'}^{i,i+1} \quad (2.65)$$

and

$$i\gamma_{nl}^{(i)} \left\{ \Theta_{nl}^{(i)} e^{i\gamma_{nl}^{(i)} \Delta z_i} - \Delta_{nl}^{(i)} e^{-i\gamma_{nl}^{(i)} \Delta z_i} \right\} \psi_{nl}^{(i)} = \sum_{n'l'} i\gamma_{n'l'}^{(i)} \left\{ \Theta_{n'l'}^{(i+1)} - \Delta_{n'l'}^{(i+1)} \right\} S_{nl,n'l'}^{i,i+1} \quad (2.66)$$

where $S_{nl,n'l'}^{i,i+1}$ denotes the overlap of the lateral wave functions in segments i and $i+1$ defined by

$$S_{nl,n'l'}^{i,i+1} = \int dx dy \psi_{nl}^\dagger(x, y, z_i) \psi_{n'l'}(x, y, z_{i+1}) \quad (2.67)$$

We note that the lateral wave functions form an orthogonal complete set in every segment. However, because of the change in the contact area, they do not have such a property in different segments. Now we will write equations 2.65 and 2.66 in a matrix form to get

$$\begin{aligned} e^{i\tilde{\Gamma}^{(i)} \Delta z_i} \tilde{\Theta}^{(i)} + e^{-i\tilde{\Gamma}^{(i)} \Delta z_i} \tilde{\Delta}^{(i)} &= \tilde{S}^{i,i+1} \left[\tilde{\Theta}^{(i+1)} + \tilde{\Delta}^{(i+1)} \right] \\ e^{i\tilde{\Gamma}^{(i)} \Delta z_i} \tilde{\Theta}^{(i)} - e^{-i\tilde{\Gamma}^{(i)} \Delta z_i} \tilde{\Delta}^{(i)} &= \tilde{\Gamma}^{(i)-1} \tilde{S}^{i,i+1} \tilde{\Gamma}^{(i+1)} \left[\tilde{\Theta}^{(i+1)} - \tilde{\Delta}^{(i+1)} \right] \end{aligned} \quad (2.68)$$

Therefore, the transfer matrix for the i^{th} interface is

$$\tilde{T}^{i,i+1} = \frac{1}{2} \left[\begin{array}{cc} e^{-i\tilde{\Gamma}^{(i)} \Delta z_i} \left\{ \tilde{S}^{i,i+1} + \tilde{\Gamma}^{(i)-1} \tilde{S}^{i,i+1} \tilde{\Gamma}^{(i+1)} \right\} & e^{-i\tilde{\Gamma}^{(i)} \Delta z_i} \left\{ \tilde{S}^{i,i+1} - \tilde{\Gamma}^{(i)-1} \tilde{S}^{i,i+1} \tilde{\Gamma}^{(i+1)} \right\} \\ e^{i\tilde{\Gamma}^{(i)} \Delta z_i} \left\{ \tilde{S}^{i,i+1} - \tilde{\Gamma}^{(i)-1} \tilde{S}^{i,i+1} \tilde{\Gamma}^{(i+1)} \right\} & e^{i\tilde{\Gamma}^{(i)} \Delta z_i} \left\{ \tilde{S}^{i,i+1} + \tilde{\Gamma}^{(i)-1} \tilde{S}^{i,i+1} \tilde{\Gamma}^{(i+1)} \right\} \end{array} \right] \quad (2.69)$$

which connects the solution in the i^{th} segment to that in the $(i+1)^{th}$ segment as

$$\begin{bmatrix} \tilde{\Theta}^{(i)} \\ \tilde{\Delta}^{(i)} \end{bmatrix} = \tilde{T}^{i,i+1} \begin{bmatrix} \tilde{\Theta}^{(i+1)} \\ \tilde{\Delta}^{(i+1)} \end{bmatrix} \quad (2.70)$$

Having found the transfer matrix which connects every two adjacent matrices, we can relate the constants in the first and the last segments through the relation

$$\begin{bmatrix} \tilde{\Theta}^{(1)} \\ \tilde{\Delta}^{(1)} \end{bmatrix} = \tilde{T}^{1,N} \begin{bmatrix} \tilde{\Theta}^{(N)} \\ \tilde{\Delta}^{(N)} \end{bmatrix} \quad (2.71)$$

where

$$\tilde{T}^{1,N} = \prod_{i=1}^{N-1} \tilde{T}^{i,i+1} \quad (2.72)$$

Now we will make use of the continuity of the wave function and its derivative at $z = 0$ and $z = d$; this is the same as a uniform constriction connected to a jellium reservoirs. Referring to equations 2.43 and 2.44 we get

$$2\pi 2k_{z_o} \tilde{\Phi}^\dagger(\vec{\kappa}_o) = (\tilde{K}^{(0)} + \tilde{\Gamma}^{(0)})\tilde{\Theta}^{(0)} + (\tilde{K}^{(0)} - \tilde{\Gamma}^{(0)})\tilde{\Delta}^{(0)}, \quad (2.73)$$

and

$$(\tilde{K}^{(N)} - \tilde{\Gamma}^{(N)})e^{i\tilde{\Gamma}^{(N)}\Delta z_N}\tilde{\Theta}^{(N)} + (\tilde{K}^{(N)} + \tilde{\Gamma}^{(N)})e^{-i\tilde{\Gamma}^{(N)}\Delta z_N}\tilde{\Delta}^{(N)}, \quad (2.74)$$

and also,

$$\tilde{\Theta}^{(0)} = \tilde{T}_{11}^{(1,N)}\tilde{\Theta}^{(N)} + \tilde{T}_{12}^{(1,N)}\tilde{\Delta}^{(N)} \quad (2.75)$$

$$\tilde{\Delta}^{(0)} = \tilde{T}_{21}^{(1,N)}\tilde{\Theta}^{(N)} + \tilde{T}_{22}^{(1,N)}\tilde{\Delta}^{(N)} \quad (2.76)$$

Here $\tilde{\Phi}^*(\vec{\kappa}_o)$ is the Fourier transform of the wave function in the first segment. Now we can solve the previous equations simultaneously to obtain the wave function in the N^{th} segment. Therefore using equation 2.16 we calculate the conductivity in the constriction with varying crosssection. In fact the solution of the conductivity is of the same form as 2.54, however, we need to make the following transformations $\tilde{\Gamma}_{R,I} \rightarrow \tilde{\Gamma}_{R,I}^{(N)}$ and $\tilde{K} \rightarrow \tilde{K}^{(N)}$, while $\tilde{\Pi}$ & $\tilde{\Lambda}$ will have the following form

$$\begin{aligned} \tilde{\Pi} &= 2 \left[\tilde{T}_{11}^{(1,N)} + \tilde{T}_{12}^{(1,N)} e^{i\tilde{\Gamma}^{(N)}\Delta z_N} \tilde{\Gamma}^{(N)} e^{i\tilde{\Gamma}^{(N)}\Delta z_N} \right. \\ &\quad \left. - \tilde{\Gamma}^{(0)} \left(\tilde{T}_{21}^{(1,N)} + \tilde{T}_{22}^{(1,N)} e^{i\tilde{\Gamma}^{(N)}\Delta z_N} \tilde{\Gamma}^{(N)} e^{i\tilde{\Gamma}^{(N)}\Delta z_N} \right) \right]^{-1} \left(\tilde{K}^{(N)} + \tilde{\Gamma}^{(N)} \right)^{-1} \end{aligned} \quad (2.77)$$

and

$$\tilde{\Lambda} = e^{i\tilde{\Gamma}^{(N)}\Delta z_N} \tilde{\gamma}^{(N)} e^{i\tilde{\Gamma}^{(N)}\Delta z_N} \tilde{\Pi}, \quad (2.78)$$

where

$$\tilde{\gamma}^{(M)} = \left(\tilde{K}^{(M)} + \tilde{\Gamma}^{(M)} \right)^{-1} \left(\tilde{\Gamma}^{(M)} - \tilde{K}^{(M)} \right), \quad (\text{with } M = 0, N) \quad (2.79)$$

Before investigating our results we note that using cylindrical potential the overlap matrix $S_{nl,n'l'}^{i,i+1}$ of lateral wave function would have a simpler form compared with the general case and we get

$$\begin{aligned} S_{nl,n'l'}^{i,i+1} &= \int_0^{\min\{w_i, w_{i+1}\}} \int_0^{2\pi} \frac{1}{\sqrt{\pi}} \frac{1}{w_i} \frac{J_l\left(u_{nl} \frac{\rho}{w_i}\right)}{J_{l+1}(u_{nl})} e^{-il\phi} \frac{1}{\sqrt{\pi}} \frac{1}{w_{i+1}} \frac{J_{l'}\left(u_{n'l'} \frac{\rho}{w_{i+1}}\right)}{J_{l'+1}(u_{n'l'})} e^{il'\phi} \rho d\rho d\phi \\ &= \delta_{ll'} \frac{2}{w_i w_{i+1}} \frac{1}{J_{l+1}(u_{nl}) J_{l+1}(u_{n'l'})} \int_0^{w_{<}} J_l\left(u_{nl} \frac{\rho}{w_i}\right) J_l\left(u_{n'l'} \frac{\rho}{w_i}\right) \rho d\rho \end{aligned} \quad (2.80)$$

where we would use the definition $w_{<} = \min\{w_i, w_{i+1}\}$ and $w_{>} = \max\{w_i, w_{i+1}\}$

and

$$J_l\left(u_{nl} \frac{\rho}{w_{<,>}}\right) = J_l\left(u_{<,>} \frac{\rho}{w_{<,>}}\right) \quad \text{where } m = n, n'. \quad (2.81)$$

Thus

$$\begin{aligned} S_{nl,n'l'}^{i,i+1} &= \delta_{ll'} \frac{2}{w_i w_{i+1}} \frac{1}{J_{l+1}(u_{nl}) J_{l+1}(u_{n'l'})} \int_0^{w_{<}} J_l\left(u_{<} \frac{\rho}{w_{<}}\right) J_l\left(u_{>} \frac{\rho}{w_{>}}\right) \rho d\rho \\ &= \delta_{ll'} \frac{2}{w_i w_{i+1}} \frac{1}{J_{l+1}(u_{nl}) J_{l+1}(u_{n'l'})} \left(\frac{w_{<}}{u_{<}}\right)^2 \int_0^{u_{<}} J_l(\rho) J_l\left(\frac{u_{>} w_{<}}{u_{<} w_{>}} u\right) u du \\ &= \begin{cases} \delta_{ll'} 2 \frac{w_{<}}{w_{>}} \frac{1}{u_{<}} \frac{J_l\left(\frac{u_{<} w_{<}}{u_{>} w_{>} u}\right)}{J_{l+1}(u_{>})} \frac{1}{1 - \left(\frac{u_{<} w_{<}}{u_{>} w_{>}}\right)^2} & \text{if } \left(\frac{u_{<} w_{<}}{u_{>} w_{>}} \neq 1\right) \\ \delta_{ll'} \frac{w_{<}}{w_{>}} \frac{J_{l+1}(u_{<})}{J_{l+1}(u_{>})} & (\text{otherwise}) \end{cases} \end{aligned} \quad (2.82)$$

2.4.2 Nanoindentation

In our model the nanoindentation is represented by a jellium substrate and jellium STM tip which has a cone angle 2α and height $4\lambda_F$. We calculate the conductance of nanoindentation as the tip is pushed continuously towards the metal substrate. Here it is assumed that A increases continuously as in the

continuum approximation to the matter, in which the excess material due to the tip indenting the surface is implemented to the cylindrical neck growing at the contact. As a result the length d of the neck at the contact increases with increasing s , the distance indented in the material. In reality, d may be even relatively smaller since A is expected to be larger near the surface. We have presented the results of our calculation for $G(A)$ and $G(s)$ in Figure 2.4. Note that due to the tunneling neither the jumps are steep nor the plateaus are flat in the G versus s curve. The important question to be addressed now is whether the steep jumps in experiment correspond to the quantization of G or not. Of course, for $A \sim \lambda_F^2$ and $d \sim \lambda_F$ the electron energies in the contact are quantized with wide level spacings. The structure of G curves is only the manifestation of this phenomenon, but does not indicate the quantization of G itself. How sharp are the steps and how close are their heights to the multiples of G_0 can be taken as a criteria for the perfectness of the "quantization" and also as the signature for the formation of individual channels. Here we should emphasize the fact that the model used in Figure 2.4 is too idealistic. The actual contact shall be relatively shorter ($d \leq \lambda_F$) and nonuniform, and shall include severe structural disorder. The quantization of electronic states do not lead to the step structure of G . Tunneling becomes important for short d and the current carrying states are back-scattered from atomic disorders. As a result, the step structure is smeared out and plateaus disappear. For strong disorder (elastic mean free path $l_e < l$), the channel openings are delayed and the step structure is shadowed by the universal conductance fluctuations.³⁹ At the end, the sharp step structure is smoother and is even faded away, but the noticeable jumps of $G(s)$ curves in the range of G_0 occur when A experiences sudden and large increase. In the experimental studies G is plotted with respect to s , since one cannot measure A precisely in the course of indentation. In reality, the dependence of A on s , i.e $A(s)$, is not a continuous function,⁴⁰ but changes only at certain values of s . Between two consecutive abrupt changes of A , G would exhibit minor variation except changes due to the relaxation of atomic structure. Consequently, the G versus s plots as presented in experimental papers generally reveal sudden and

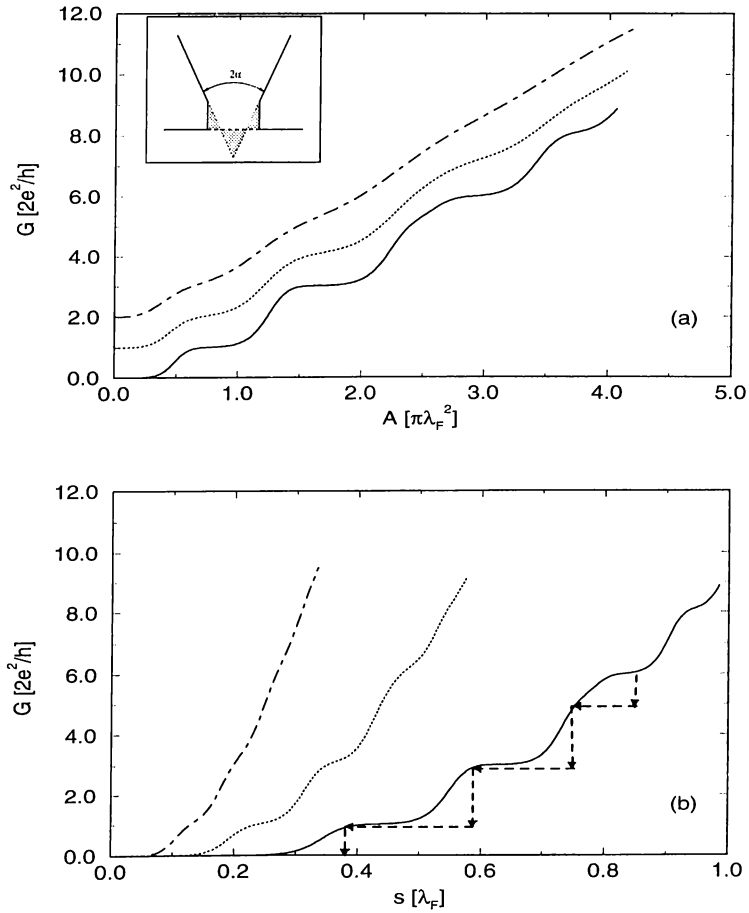


Figure 2.4: Conductance G versus cross section (a), and G versus displacement or push s (b) calculated for nanoindentation described in the inset. Dash-dotted, dotted and continuous lines correspond to $2\alpha = 120^\circ$; 90° and 60° , respectively. Cone angle $2\alpha \sim 60^\circ$ corresponds to a STM tip in the (111) orientation. Dashed line is the schematic description of the variation of $G(s)$ upon the discontinuous change of the cross section while pushing. In (a), $G(A)$ curves are up-shifted for clarity.

much steeper jumps when A experiences abrupt changes; and this is represented by a schematic description of the variation of $G(s)$ upon the discontinuous change of the cross section while pushing.

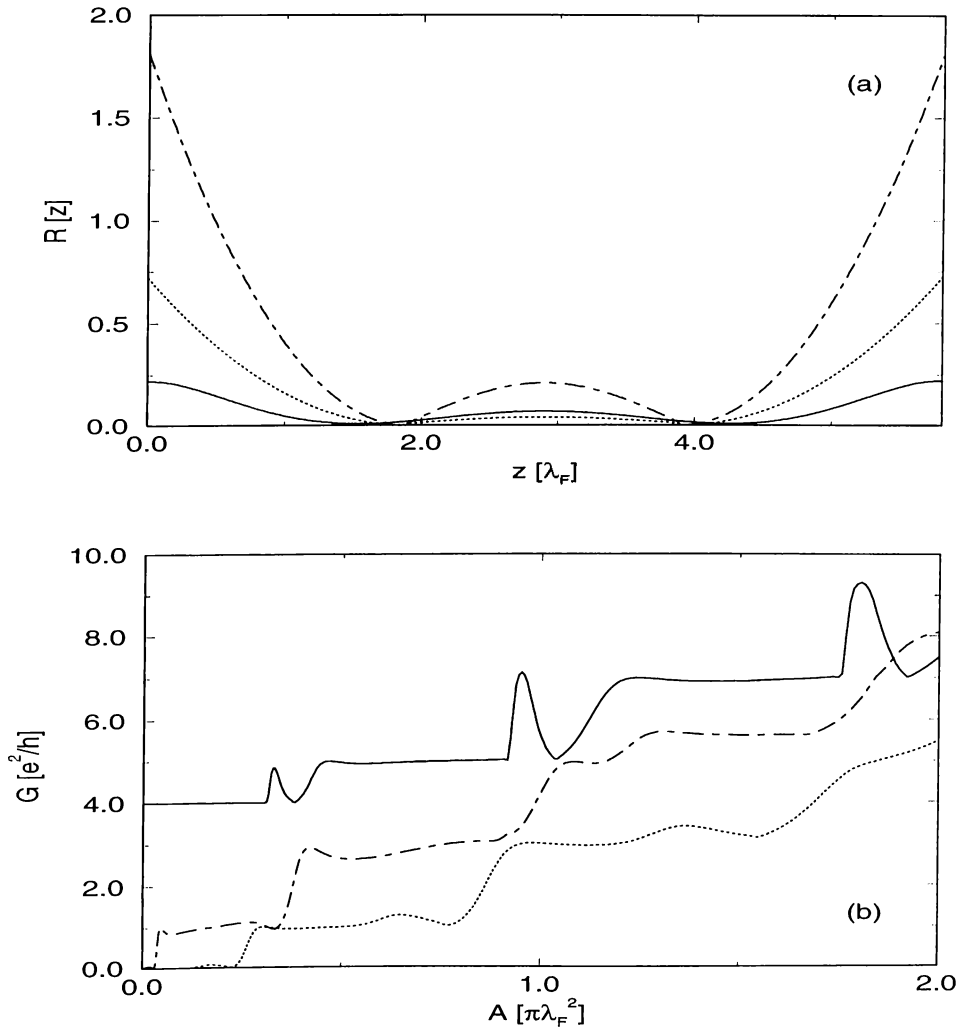


Figure 2.5: Resonant tunneling effect in the neck inducing spikes on the plateaus. (a) The surface profiles $R(z)$, of the neck used in the calculations. (b) G versus cross section A , calculated for surface profiles in (a). For A , the narrowest cross section is taken; and the the solid line is up-shifted by $4G_o$ for clarity in (b).

2.4.3 Resonant Tunneling

We have seen that in ballistic transport, whenever a subband energy ϵ_{nl} is below E_F , it contributes to conductivity with $\sim 1G_o$ or $\sim 2G_o$ depending on the degeneracy of the subband. Now, we would think of widening the constriction at the center ($z = d/2$), therefore we would form a cavity (effective potential of which resembles to a quantum well) along the channel. Thus the constriction acts like a quantum well between two potential barriers for certain *QPC* configurations.

Such a structure leads to the formation of eigenstates at the center of the constriction which are bound to the cavity. In fact our molecular dynamics simulations and previous ones³⁸ indicate that connective neck can be widened locally in the course of stretch. While the form and size of the local widening is modified in the course of the yield, a bound state may become aligned with E_F temporarily. This way the necessary conditions are realized for resonant tunneling to occur as in the double barrier resonant structure (DBRT). As a result, a peak is formed on the plateau of the $G(s)$ curve before the threshold of a new fall. Since we do not know the actual variation of the local widening (it is too much experimental condition dependent), we illustrate the resonant tunneling effect by varying the diameter of the whole neck keeping the form (or surface profile) invariant in Figure 2.5-a. The calculated G vs A curves are shown in Figure 2.5-b. From these graphs, we note that the structure which corresponds to dot-dash curve merge to a plateau because it gives rise to several adjacent resonance structure; while that due to the continuous line representation (top curve in conductivity) is well resolved. On the other hand, the bottom curve, also reveals some resonance structure but it is hidden because it is occurring adjacent to the plateau.

Chapter 3

Yielding and Fracture Mechanics of Nanowires

3.1 Motivation

In the previous chapter, we have studied throughly ballistic transport in small structure; and we have seen that direct generalization of the energy quantization phenomenon in *2DEG* to the *3D Q.P.C.* may explain some structural features of the conductivity such as the stair case feature with multiples of $2e^2/h$. However it fails for most of the other behaviors such as dips, subquantum steps, positive and negative slopes on the plateaus. We believe that the discrete nature of the wire is essential for various features observed experimentally. Therefore, a through analysis of the atomic structure as a function of stretch is necessary. In fact, recent experiments⁴¹⁻⁴³ providing simultaneous measurements of force and conductance variations have shown that the observed jumps in conductance are connected with the sudden jumps in measured force. This phenomenon was predicted much earlier by Ciraci and Tekman,¹³ who proposed that the sudden changes of G over the smooth Sharvin's conductance originate from the discontinuous variation of the contact area.

The narrowest diameter of the nanowire prior to the break is only a few angstrom or $\sim \lambda_F$, where discontinuous (discrete) nature of the metal dominates over its

continuum description. For example, in this length scale, the level spacings of electrons ($0.1 - 1\text{eV}$) become easily resolved even at room temperature, and any change of atomic structure may lead to detectable changes in the related properties. It becomes now clear that the yielding mechanisms of the nanowires are quite different from those of macrowires displaying bulk properties. The unusual plastic deformation of a connective neck under tensile stress and resulting discontinuous force variations were first predicted by Landman *et al.*⁴⁰ Subsequently, the mechanical properties of nanowire during pulling attracted interest.^{38,44}

Various electronic processes, which resulted from elastic and plastic deformations of a nanowire are not fully understood yet and deserve further study. Therefore we have investigated yielding and fracture mechanisms of nanowire which is pulled by an external agent. To understand the origin of these mechanisms and abrupt force variations, we also performed an extensive analysis of atomic structure in the course of pulling. In particular, we followed the motion of the neck atoms and examined their symmetries and coordination numbers during the abrupt force variations. We also investigated the effect of temperature, initial size (neck diameter) and shape of the nanowire, with length increments used in simulation (Δl). We used both embedded atom (EA)⁴⁵⁻⁴⁷ and 2-body pair potentials,⁴⁸ and carried out simulations based on molecular dynamics method.³³

3.2 Molecular Dynamics Simulation

3.2.1 Investigated Parameters

In our simulations, we define an interatomic potential which is responsible for the atomic motion and cohesion. The interatomic potentials are described by empirical potential functions. Here we used 2-body pair potential (PP) as well as embedded atom model.

Concerning the PP, we used empirical many body potential energy function constructed in terms of pair potential⁴⁸ interaction and it was applied to Cu bulk

$A_1 =$	110.76608	$A_2 =$	-46.164783
$\lambda_1 =$	2.09045946	$\lambda_2 =$	1.49853083
$\alpha_1 =$	0.394142248	$\alpha_2 =$	0.20722507
$D_{21} =$	0.436092895	$D_{22} =$	0.245082238

Table 3.1: Constants used to define Pair Potential.

material and it was shown that this potential gives fcc as the most stable structure for bulk Cu, as well as physical quantities were comparable with experimental ones. However, the only handi-cap of this potential is that it predicts a positive relaxation of interlayer distance at the surface. The potential has the form

$$\begin{aligned} \Phi &= D_{21}\phi_{21} + D_{22}\phi_{22} \\ \text{where } \phi_{2k}(r) &= A_k e^{-\lambda_k} e^{-\alpha_k r^2} \end{aligned} \quad (3.1)$$

with values of A 's, λ 's, α 's and D 's presented in table 3.1, and the energy is in eV and distance in \AA .

The other potential we used is obtained from the embedded atom model which is a many particle potential. In fact such potential types have been introduced with the work done by M.S. Daw *et al.*⁴⁵ In this formalism, one writes the total energy of the system as

$$E_T = \sum_i F_i(\rho_{h,i}) + 1/2 \sum_{i,j(i \neq j)} \phi_{ij}(R_{i,j}) \quad (3.2)$$

where

- $\rho_{h,i}$ is the host electron density at atom i due to the remaining atoms of the system defined by: $\rho_{h,i} = \sum_{j \neq i} \rho_j^a(R_{ij})$ with $\rho_j^a(R)$ is the electron density contributed by atom j at distance R .
- $F_i(\rho)$ is the energy needed to embed atom i into the background electron density ρ .
- ϕ_{ij} is short range (doubly screened) core-core pair repulsion between atom i and atom j separated by distance R_{ij}

In the paper by S. M. Foiles *et al.*,⁴⁶ the equation for the total energy parameters are empirically determined for the case where ρ may diverge from ρ_{eq} (charge density of the bulk sample). They take the core potential as

$$\phi_{AB}(R) = \frac{Z_A(R)Z_B(R)}{R} \quad (3.3)$$

$$\text{where } Z(R) = Z_o(1 + \beta R^\mu)e^{-\alpha R} \quad (3.4)$$

and for Cu they take $Z_o = 11$, $\alpha = 1.7227$, $\beta = 0.1609$ and $\mu = 2$. The atomic electron density was computed from Hatree-Fock wave functions by

$$\rho^a(R) = n_s\rho_s(R) + n_d\rho_d(R) \quad (3.5)$$

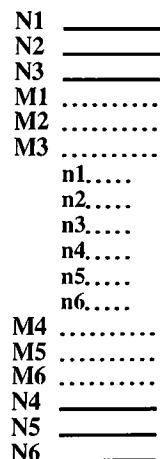
and for Cu $n_s = 1$ and $n_d = 10$.

Once the electron densities $\rho_j^a(R)$ and core interaction $\phi(R)$ are both known, we can determine $F(\rho)$ uniquely because the total energy of the homogeneous fcc solid computed with E.A potential has to fit the simple universal function⁴⁹

$$E(a) = -E_{sub}(1 + a^*)e^{-a^*} \quad (3.6)$$

where E_{sub} is the absolute value of the sublimation energy at 0 temperature and pressure; and a^* measure the deviation from the equilibrium lattice constant. Therefore, getting $\rho(R)$ and $F(\rho)$ numerically (which was supplied by M. S. Daw), we can generate our potential and use it for our simulations.

Having discussed the potential parameters used in our simulations, we next present the different structures we have investigated. The nanowires we studied have two ends which are connected by a neck, and have quasi circular crosssection. The description of the structure are summarized in Figure 3.1. Last three layers at both ends (N_1, N_2, N_3 and N_4, N_5, N_6) are fixed. The position of the atoms in these layers are translated along the stretch direction only by the increment Δl , otherwise they are fixed during the MD-steps. These fixed three layers at each end are assumed to be connected to the external agent which applies the tensile stress. Atoms in the following three layers adjacent to the fixed ones (M_1, M_2, M_3 and M_4, M_5, M_6) and those of the neck ($n1, n2, n3, n4, n5$ and $n6$ [if it exists]) are fully relaxed. We considered the "wide-neck" (WN) and "thin-neck" (TN)



Wire	Layer	N1 N2 N3	M1 M2 M3	n1 n2 n3	Layer	Poten.
		N4 N5 N6	M4 M5 M6	n4 n5 n6	Struc.	
WN1		145 144 145	144 145 144	13 12 13	Cu(100)	EA
		145 144 145	144 145 145	12 13		
WN2		145 144 145	144 145 144	13 12 13	Cu(100)	PP
		145 144 145	144 145 144	12 13		
WN3		143 143 143	143 143 143	12 12 13	Cu(111)	EA
		143 143 143	143 143 143	12 12 13		
TN1		41 40 41	40 41 40	5 4 5	Cu(100)	PP
		41 40 41	40 41 40	4 5		
TN2		41 40 41	40 25 12	5 4 5	Cu(100)	PP
		41 40 41	12 25 40	4 5		

Figure 3.1: Description of different structures used in the simulation.

structures. The nanowire indicated *WN1* is formed from Cu(100) atomic layers; the interatomic interactions are treated by the EA model. The wire itself is represented by a periodically repeating system in the x - y plane. The z -axis is taken to be parallel to the axis of the nanowire. The interatomic interactions in the nanowire *WN2*, in the thin nanowires *TN1* and *TN2* are treated by pair-potentials. We have also investigated a nanowire having Cu(111) orientation surface with EAM in *WN3* at $T = 300K$. Having seen that both potentials, embedded atom potential and pair potential revealed the same general features, we used pair-potentials (which is relatively faster) to explore various effects. The pulling (stretch) is realized by displacing the fixed layers (N 's) from one end by Δl or from both ends (for *TN2* only). Subsequently, the atoms of the wires (M 's and n 's) are relaxed to find their new positions.

3.2.2 Molecular Dynamics Method

In our MD simulations, we were pulling top fixed atoms ($N1$, $N2$ and $N3$) by a distance $\Delta l = 0.1\text{\AA}$ and then relaxing all the atoms at the neck, M 's and n 's. The relaxing phenomenon is proceeded by solving Newton's equation of

motion for every atom after finding out its interaction potential with the rest of the system either with PP or EA. Here we used cut-off radius (R_c) 10\AA for PP and 4.5\AA for EA. These R_c values were chosen by convergence tests. During the relaxation process, we took very short time steps $\Delta t \sim D_t/100 \sim 10^{-15}s$ to integrate Newton's equation. In such a short time interval, we can assume that the force exerted on every atom is constant and we get

$$\begin{aligned} V_k(t_f) &= V_k(t_i) + \frac{F_k(t_i)}{m}(t_f - t_i) \\ X_k(t_f) &= X_k(t_i) + V_k(t_i)(t_f - t_i) + \frac{F_k(t_i)}{2m}(t_f - t_i)^2 \end{aligned} \quad (3.7)$$

where the subscript k denotes the k^{th} atom in the system. t_f and t_i denote the final and initial times respectively, with $\Delta t = t_f - t_i$, is the integration time step; $F(t_i)$ is the force exerted on the atom at the initial time; and X, V correspond to the position and velocity of the atom at the corresponding times, respectively. In these simulations, we are neglecting all scattering phenomena in the system; to avoid divergence of kinetic energy of moving atoms, we rescale it to $3Nk_B T/2$ every two steps. Here N is the number of moving atoms, k_B is Boltzmann constant and T is the temperature. We integrate Newton's equation (3.7) over large number of time steps until convergence is reached. Convergence criteria is tested by removing the rescaling process and checking that the kinetic energy is roughly constant after many steps (~ 1000); this suggests that the atoms have been trapped at a local minimum and we are ready for the next step for pulling. The appropriate time step for integration Δt and the total number of integration steps can only be investigated through tests, because it may change from one system to another. In table 3.2 we present the corresponding parameters

WIRE	Δt	# of steps	averaging
WN1	$0.1 \times 10^{15}s$	25000	8333
WN2	$0.9 \times 10^{15}s$	6000	2000
WN3	$0.5 \times 10^{15}s$	7000	2333
TN	$0.9 \times 10^{15}s$	8000	2000

Table 3.2: Description of different parameters used for systems relaxation.

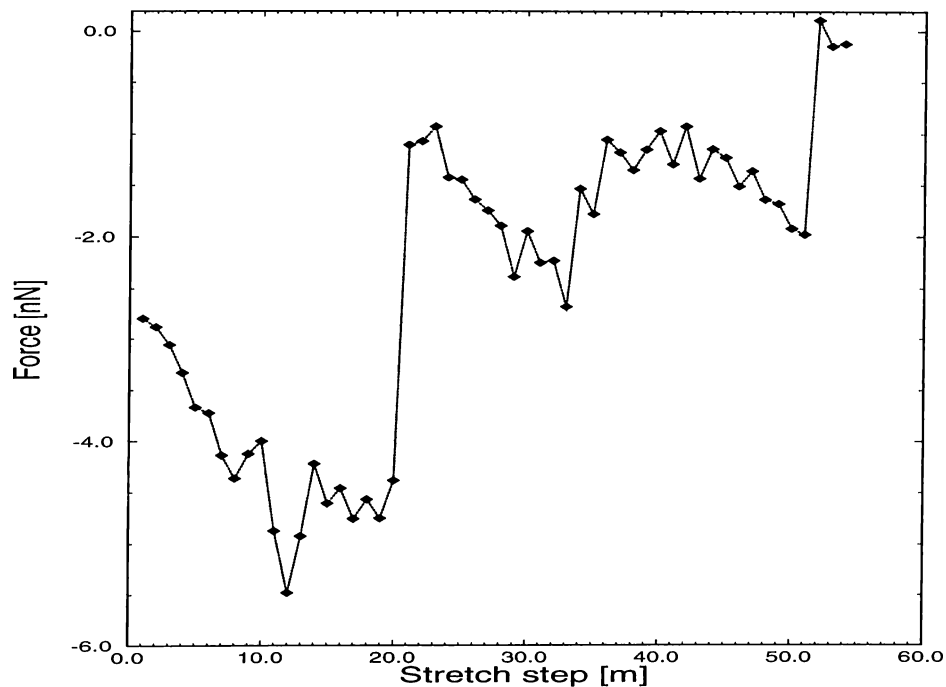


Figure 3.2: Interaction force between the top three layers ($N1$, $N2$ and $N3$) and the rest of the system.

used for relaxation.

In order to calculate any physical quantity (such as force exerted on some atoms), we have to use averaging procedure during our computation. Here, we note that our time scale is very short compared to the experimental time scale. For this reason, we take an average value over a large number of time steps ($\sim 1/3$ of the relaxing time interval) occurring towards the end of relaxation while measuring physical quantities. In table 3.2 we give the corresponding numbers for averaging.

3.3 Results and Discussion

3.3.1 Nanowire $WN1$

We examine first the elongation and various physical events during the stretch of the nanowire, $WN1$ at $T = 300K$. Simulations are performed by using EA potential. In Figure 3.2, we illustrate the variation of F_z (The interaction force of the top 3 fixed layers $N1$, $N2$ and $N3$ with the rest of the system) as a function

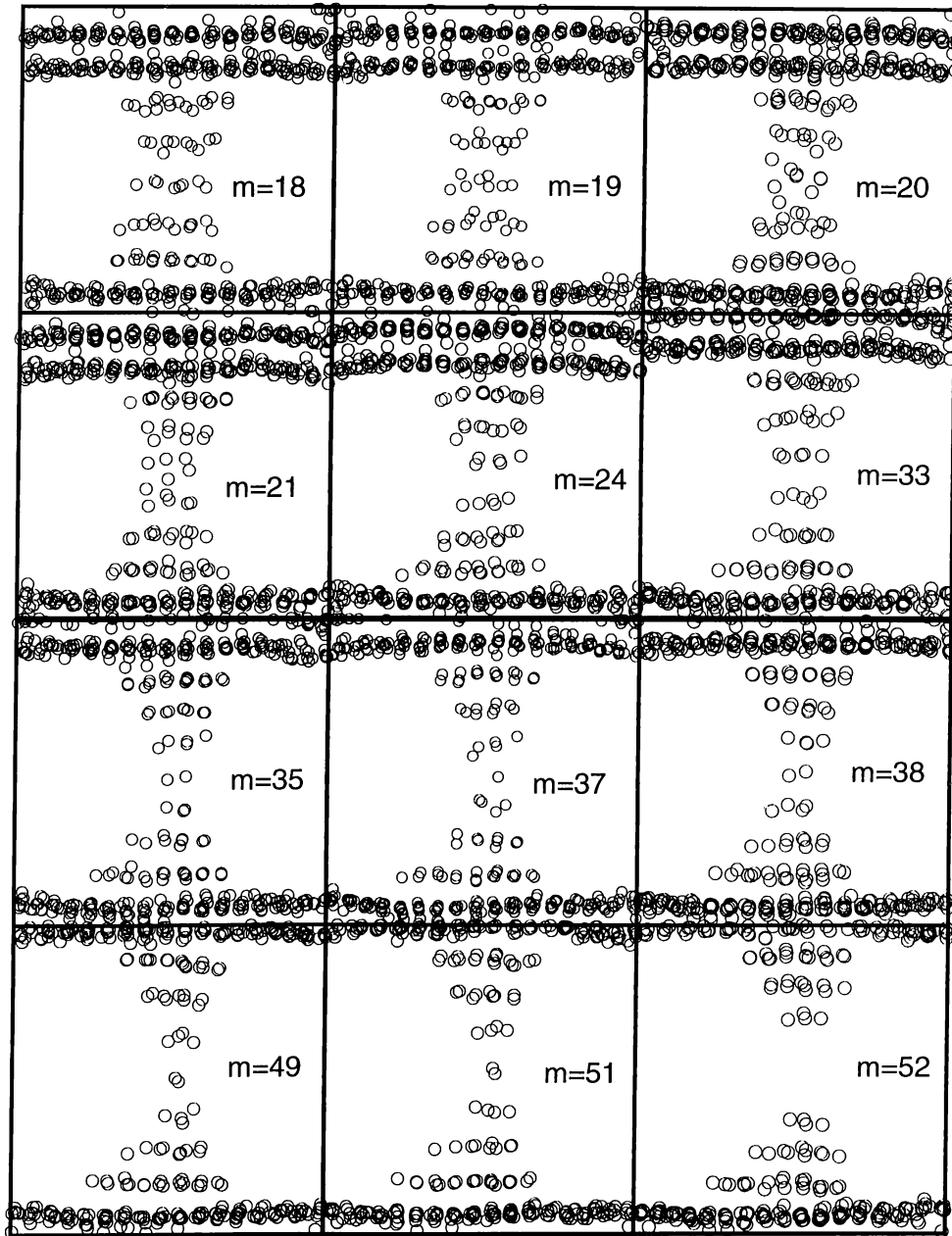


Figure 3.3: Side view of the neck atoms at some specific stretch increments $m\Delta l$.

of stretch $m\Delta l$ (m , being an integer multiples of increment). Figure 3.3, shows the side view of atomic structure at the neck at some specific stretch increments. The $F_z(m)$ curve shown in Figure 3.2 displays interesting features that are worth

to be mentioned and discussed. The magnitude of the average force increases “smoothly” with increasing m between two consecutive jumps, but it decreases at each jump. The graphical representation indicates that a jump occurs whenever approximately 18 increments of stretch are made. This value (which is $\sim 1.8\text{\AA}$) corresponds to the interlayer spacing of $c = a/2 = 1.81$. Stated differently, *the tensile force makes a sudden jump* whenever the length l of the nanowire is elongated by approximately an interlayer distance. The jump of $F_z(m)$ starts as the atomic structure of the neck becomes irregular, and lasts until a new layer with relatively smaller crosssection is generated. We now examine various physical phenomena in detail.

As we are pulling the top 3 layers and relaxing the neck atoms, the layer structure becomes stable and it can be very well distinguished up to $m \sim 18$ (We could observe only migration of few atoms from the neck to form horn like structure with 8 atoms at the center). After this point, at $m = 19$ (the last increment before the jump in $F_z(m)$), the layer structure is destroyed and becomes amorphous (as shown for $m = 20$ in Figure 3.3). The layer structure is recovered after a few increments, at $m = 24$ with the creation of a new layer. At the end of this transformation, the crosssection of the neck is reduced from 8 atoms to 5 atoms, whereas the crosssections of neck layers adjacent to the end layers ($n1$ and $n5$) are not altered. The local reduction of the crosssection due to stretching causes $|F_z|$ to reduce, and hence the outer layer spacings between M_3 and $n1$ (and similar spacing at the other end) to decrease.

The layer structure of the neck is conserved in further stretch until $m = 33$. Beyond that point, each increment of stretch by Δl causes one atom from the central layer to migrate and stay in the interlayer spacing which already became wide open due to pulling from $m = 25$ to $m = 33$. This way a new “layer” with 2 atoms is formed at $m = 35$ as shown in Figure 3.3. Owing to the repulsive force induced between layers, $|F_z|$ decreases abruptly. Moreover, the crosssection of the connective neck is further reduced with central layers including 5,2,3 atoms, respectively. In the steps from $m = 35$ to $m = 38$, we note a transient event which is relevant for transport properties: One of the two atoms in the neck layer

created at $m = 35$, jumps back to the layer it emerges (Figure 3.3) at $m = 37$. During the following increment, the single atom neck is strength by the inclusion of one atom from another layer so that the necking becomes uniform by the layers including 4,2,4 atom at the central part of the neck. Due to this exchange of one atom, the conductance is expected to get a dip, which in fact has been observed. The two-atom neck is very stable and it continues until the break, at $m = 52$. Towards the end of the pulling, starting from $m = 44$, two atoms rotate in the $x - y$ and become slightly inclined in the z -direction ($m = 49$). Such a fluctuation in configuration, is expected to give rise to changes in the conductance just before the break. To understand this process better, we will come back to this point while we are studying lateral configuration. Finally we note that the narrowest crosssection of the neck prior to the break is having two atoms.

These results point to the fact that the structural transformations followed by the abrupt change of $|F_z|$ result in necking; an additional layer is formed and the narrowest crosssection decreases usually by more than one atom. In addition to these abrupt changes, we find another mechanism in necking which gives rise to relatively smaller changes in crosssection (by one atom) and it corresponds to atoms migration from the neck towards $M3$ and $M4$.

Having discussed the structural transformations within atomic layers, which are apparently non-planar and exhibit smooth distribution along the z axis, we investigate structural changes in the lateral plane. In our study, we have found that up to $m = 12$, the Cu(100) structure in the neck was having very small and random deformation (the displacements of atoms are less than 10% and no preferable direction is detected, especially those atoms without surface interaction) is detected as shown in Figure 3.4. However, surface atoms of the neck were having a slight tendency to move towards the center of the neck, this is due to the minimization of surface energy. Beyond this stretch point, the neck atoms start to build up a structure which deviates from A-B sequence of Cu(100) and this deformation starts earlier at the neck center (n_2, n_3 and n_4) at $m = 15$. In fact, this discrepancy includes two aspects, the interatomic separation distance has slightly increased (dominant mainly for the central layer) and the 2D

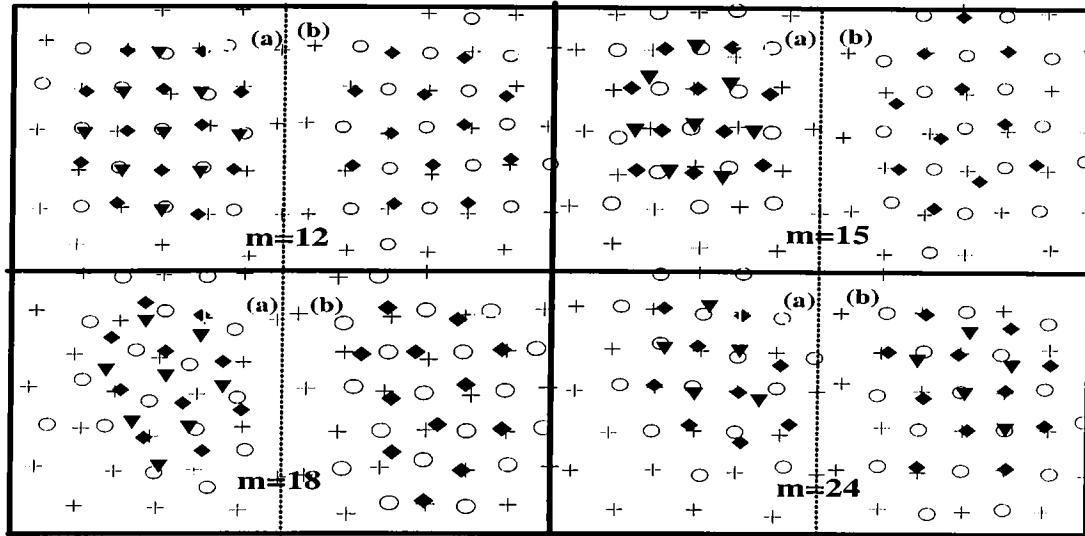


Figure 3.4: Lateral atomic structure in the neck at different stretch increments defined by the corresponding m values. In panel (a), we show the top 4 layers ($M3, n1, n2$ and $n3$) and in panel (b) we show bottom layers starting from $M4$ until $n4$.

In (a) we denote $M3, n1, n2$ and $n3$ by *plus sign, circle, diamond and down triangle*, respectively. In (b) we follow the same sequence for the bottom neck layers starting from $M4$ until $n3$.

square unit cell transforms to a hexagonal one; as shown in Figure 3.4. Following these changes, at $m = 18$ all the neck atoms have been affected by elongation of the neck, and they undergo the structural transformation which has occurred previously at $m = 15$ for central neck atoms. After the jump in the force $|F_z|$, which corresponds to the birth of a new layer \ddagger at $m = 24$, Cu(100) layer structure has been recovered at the end layers of the neck (n_1, n_2 and n_5, n_6), while atoms at the central part of the neck and at the surface still deviate from the original bulk structure as shown in Figure 3.4. This mismatch with the Cu(100) structure at the center of the neck is due to the additional *one* layer (number of layers produced is odd) introduced, and as a result it becomes impossible to follow A-B sequence of the Cu(100) and match this type of layer structure with the bulk

[‡]we would enumerate the neck layers by $n_1, n_2 \dots n_6$

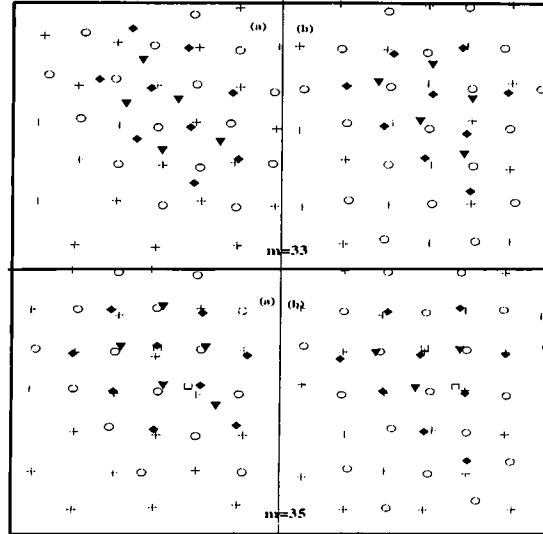


Figure 3.5: Lateral structure at $m = 33$ and $m = 35$. It is obvious how the lateral structure is destroyed before the jump in $F_z(m)$ (at $m = 33$) and recovered after a new layer is formed ($m = 35$). Now the number of layers introduced is *two*. The layer structure presentation is the same as in the previous Figure and only for $m = 35$ we use *square* symbol to denote the new layer at neck center.

layers (M3 and M4). Therefore, at $m = 24$, eventhough the 2D square unit cell is likely to be recovered at the central part of the neck, atoms move laterally to withstand this mismatch. We note that this deformation occurs mainly at the center of the neck, because here, bulk influence is minimum.

Upon further stretch, layer structure, which is less stable compared to configuration before the force jump, has been lost again at $m = 33$ and then immediately recovered at $m = 35$, also with the recovery of the original Cu(100) sequence as shown in Figure 3.5. The new layer structure is asymmetric as mentioned above, and with further migration of atoms, a more stable structure is built at $m = 38$. In this configuration we are having only *two* atoms at the central neck layer and they are not enough to define layer structure. In fact we have noticed while all the other neck atoms keep the Cu(100) structure, these ones undergo some lateral displacement that may be worth for investigation. In Figure 3.6, we show the lateral positions of only the central layers of the neck ($n3$,

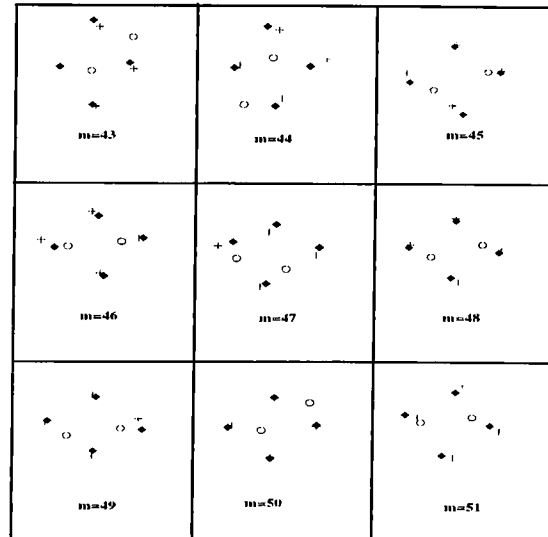


Figure 3.6: Lateral structure of neck central region to observe the bundle formation before the break of the neck.

We present layers $n5$, $n4$ and $n3$ by *plus sign*, *circle* and *dianmond*, respectively.

$n4$ and $n5$), from the $m = 43$ up to $m = 51$ (just before structure break). Here we note that except at point $m = 50$, the structure is tending to form *two* bundles. Stated differently, the two atoms in layer $n4$ (represented by *circle* in Figure 3.6) tend to align themselves with atoms in the layers above and below them ($n3$ and $n5$). The bundles form (atom alignment) is improving as a function of pulling. In fact this type of lateral motion may help us to understand the positive slope observed experimentally just before the break of neck (Figures 1.5 and 1.6). As we are pulling neck atoms at the smallest contact area align themselves to form a $1D$ chain structure which result in maximum conductivity.

The only handi-cap of this explanation is what we are observing at step $m = 50$, and in this configuration structure deviates from the bundle form. We think that this can be due to thermal fluctuations and this problem can only be resolved by taking a large number of averaging after relaxation of the system is reached.

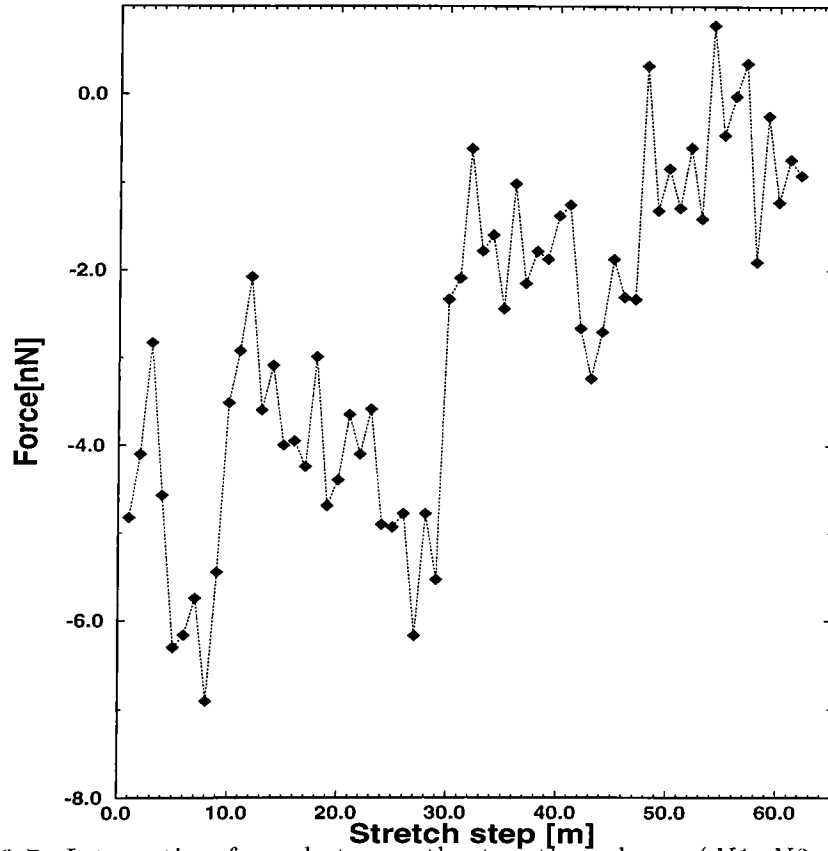


Figure 3.7: Interaction force between the top three layers($N1, N2$ and $N3$) and the rest of the the system for $WN2$.

3.3.2 Nanowire $WN2$

We will examine the simulation on the previous structure with PP while keeping all other conditions ($\Delta l = 0.1\text{\AA}$, $T = 300K$); this corresponds to $WN2$ simulations. The force, $F_z(m)$ versus stretch plot is shown in Figure 3.7. This curve exhibits some fluctuations and abrupt jumps at $m = 11$, $m = 30$ and $m = 49$, corresponding to increments of length close to the interlayer spacing of Cu(100) structure (except for the first jump). We note that these results are qualitatively the same as those obtained in Figure 3.2 using EA potential. As a result we would expect similar atomic transformations in the structure. Investigation of the nanowire show that the abrupt jumps in the $F_z(m)$ curve yield to an additional layer at the neck with smaller crosssection. This phenomenon is illustrated in Figure 3.8, in which we can see how the structure becomes

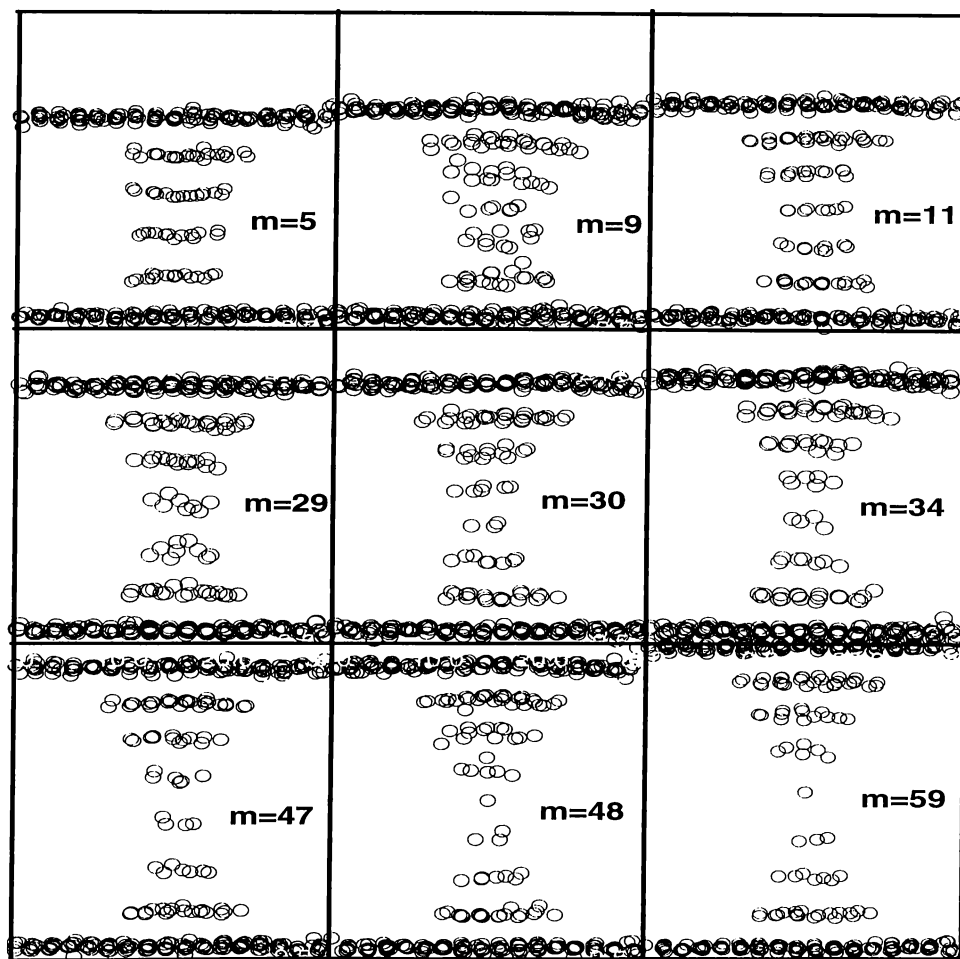


Figure 3.8: Side view of the neck atoms at some specific stretch increments $m\Delta l$ for $WN2$.

amorphous and is recovered with an additional layer at the neck. In the new configuration, the crosssection of neck center is decreased. However, the structural changes in $WN2$ are not exactly as those for $WN1$. For example, at the starting of the simulation in $WN2$, one neck layer has disappeared. This is due to the larger interlayer separation distance favored by the PP near the surface, as mentioned previously. The missing of this layer has altered the lateral layer structure which deviates from Cu(100) structure. After recovering this layer, at $m = 11$, the lateral structure has also been recovered and it became stable (the registry of the lateral structure is kept up to $m = 23$). Another important difference relative to $WN1$, is occurring towards break of the neck. In $WN2$ system, only *one* atom

exits at the neck before the break. Of course, this suggests that the cross-section of the neck is smaller than in *WN1* and as a result the conductivity for the last plateau (just before break) would be smaller by a factor $\sim 50\%$. This can be the reason why in some experiments we see a conductivity of $\sim G'_o$ while in others $\sim 2G'_o$ in the last plateau.

Next we concentrate on the structure just before the break of the neck. At stretch increment $m = 48$, one atom enters into the center of the neck and we get central layers configuration $n3, n4$ and $n5$ with 6, 1 and 3 atoms, respectively. This configuration is very stable and it continues until the neck is broken, at $m \sim 59$. During this stretching sequence, neck atoms in layers $n1, n2, n3, n6$ and $n7$ are in registry with the Cu(100) structure. However, atoms at the central region of the neck, $n4$ and $n5$ perform some lateral fluctuations due to minute bulk effects and the small number of planar atoms which cannot define layer structure. In Figure 3.9, we show atomic positions in the layers $n3, n4$ and $n5$ for various stretch increments before the neck breaks. At the beginning of stretch increments, from $m = 50$ to $m = 55$, the central atom (represented by a circle in the Figure), tends to have a hallow site configuration. Within further stretch, starting from $m = 56$, this atom changes its configuration to the top site and a bundle structure is formed at the center of the neck. Unlike nanowire *WN1*, where the two central atoms migrate from the neck center to the bulk; the one atom configuration in this structure seems to be quite stable. The atom keeps its position even after the neck is broken. Therefore it seems that Cu atom between two slabs with separation distance approximately equal to interlayer spacing, prefers the hallow site and it is quite stable. Within further pull (or increase of separation distance of the slabs), the binding energy increases and at a certain separation distance, the top site become favorable (with lower energy). In fact some calculations were performed previously on Al(001) slab and tip (only one atom at apex) with self-consistent-field calculations (SCF).⁵⁰ The results showed that for a separation distance between the slab and tip (\sim interlayer spacing), the hallow site is favorable and stable. However, as the separation distance increases, the binding energy also increases and after a pull $\sim 0.5\text{\AA}$ the top site becomes

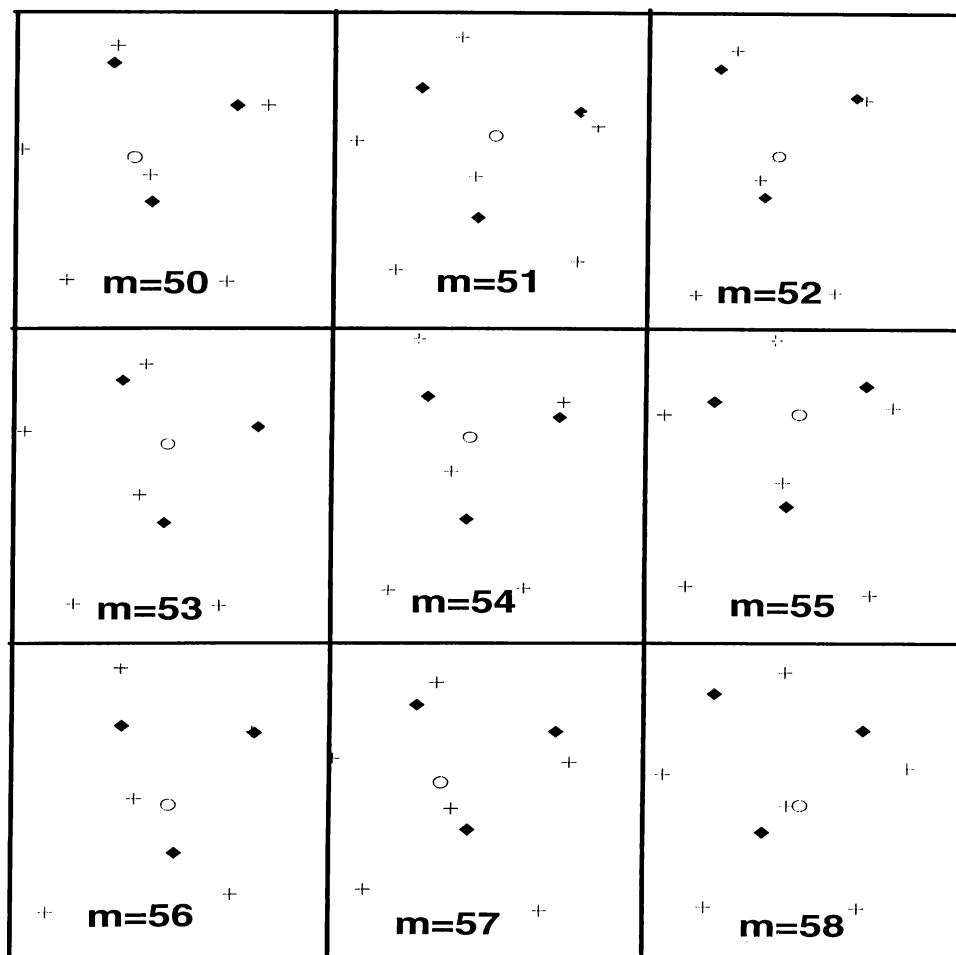


Figure 3.9: Lateral structure of neck central region towards the break of the neck. We present layers n_3 , n_4 and n_5 by *plus sign*, *circle* and *dianmond*, respectively.

favorable. Eventhough, these SCF calculations were made on a different material, we think that it can explain well the configuration that is occurring in our system before the neck breaks.

3.3.3 Nanowires TN

We have shown previously that qualitative features in the atomic fracture is the same for EA and PP. Therefore, in order to investigate other parameters, we have decided to use PP which requires shorter computer time. We have initially investigated the structure effect. We have made our MD simulations on nanowire

TN1 (which is much smaller than the previous ones) at $300K$. The general features, were the same as those of wire *WN2*. Initially, the wire was relaxed to give 4 layers at the neck. The first two jumps in the force curve correspond to the amorphisity in the system followed by the formation of a new layer at the neck center with smaller crossection. The third jump was related to the break of the neck. The configuration of the central region of the neck before it breaks was composed by 4 layers having atoms 7,1,2 and 7. This configuration was very stable, it has survived for 10 stretches. Finally we note that there were only two layers introduced at the neck; this is due to the small number of atoms at the crossection of the neck.

We have also investigated the effect of stretch increment on the nanowire *TN2*. In order to decrease simulation time, we have decided to stretch our sample from both sides by increments Δl . We have investigated *three* different increments $\Delta l = 0.05\text{\AA}$ (which corresponds to stretch of 0.1\AA from one side), 0.1\AA and 0.15\AA . The force curve for the first two values of Δl (0.05\AA and 0.1\AA) gave nearly the same results. The jump in the curve was corresponding to the formation of a new layer after a stretch length $\sim 1.9\text{\AA}$, and the neck has broken after stretch of $\sim 3.6\text{\AA}$ (Total length in both directions) for both stretching increments. However, for the last increment length scale, $\Delta l = 0.15$, no jump in the curve was observed and no layer was produced. The force curve was varying smoothly in a parabolic shape until the nanowire breaks at early stage from the neck center. From these results, we understand that there exists a limit for the stretch increment $\Delta l \sim 0.1\text{\AA}$ from both ends. This corresponds to the maximum tensile force (or max speed of withdrawing a tip from sample) above which neck breaks before showing any layer structure variation. In all our previous simulations, we were using an increment $\Delta l = 0.1\text{\AA}$ from only one edge. This suggests that our results, the calculations we draw there form are reliable.

Finally we have investigated the effect of temperature on small systems while pulling them. Therefore we have made simulations at $1K$ for structure *TN2* with stretching length of $\Delta l = 0.1\text{\AA}$. We have allowed this structure to relax for a longer time (24000 steps) because of its small kinetic energy. In Figure 3.10, we

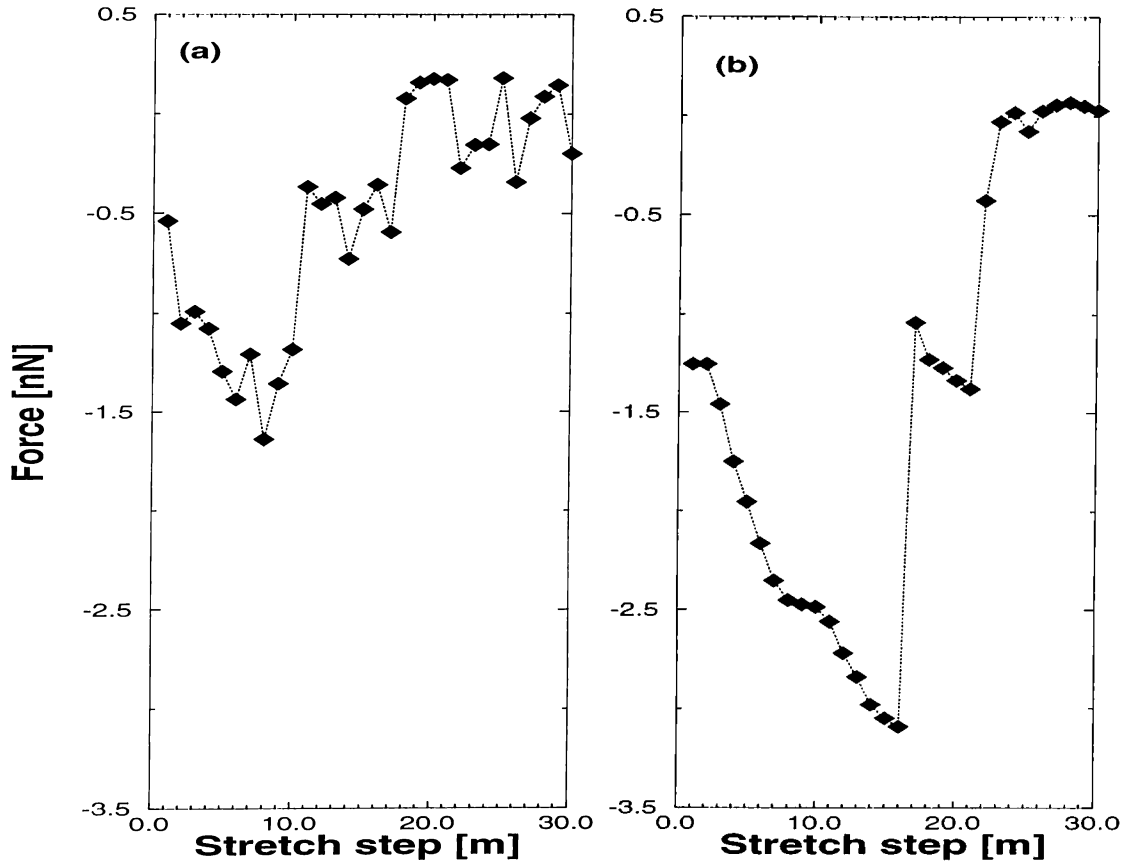


Figure 3.10: Force versus stretch increment $m\Delta l$ for nanowire $TN2$, with stretching length increment $\Delta l = 0.1\text{\AA}$ from both ends and Temperature $300K$ (a), and $1K$ (b).

show the force versus stretch for $TN2$ nanowire at $T = 300K$ and $T = 1K$. The first striking phenomenon is that thermal fluctuations have diminished completely in the plot obtained at $T = 1K$. The step structure in this curve is much sharper than the one corresponding to $T = 300K$. We also note that subsequent jumps in the force curve occur at a large stretch interval for $1K$ calculations than that at $300K$. This has induced a stronger attractive force. While we are investigating the atomic structure of these systems we have noticed that at $T = 1K$, structure stays amorphous nearly all the way before inducing the first layer. This discrepancy can be explained by the fact that at low T , the kinetic energy is small enough that atoms are trapped easily in local minima energies. Therefore, larger stretching distance is required in order to separate atoms from

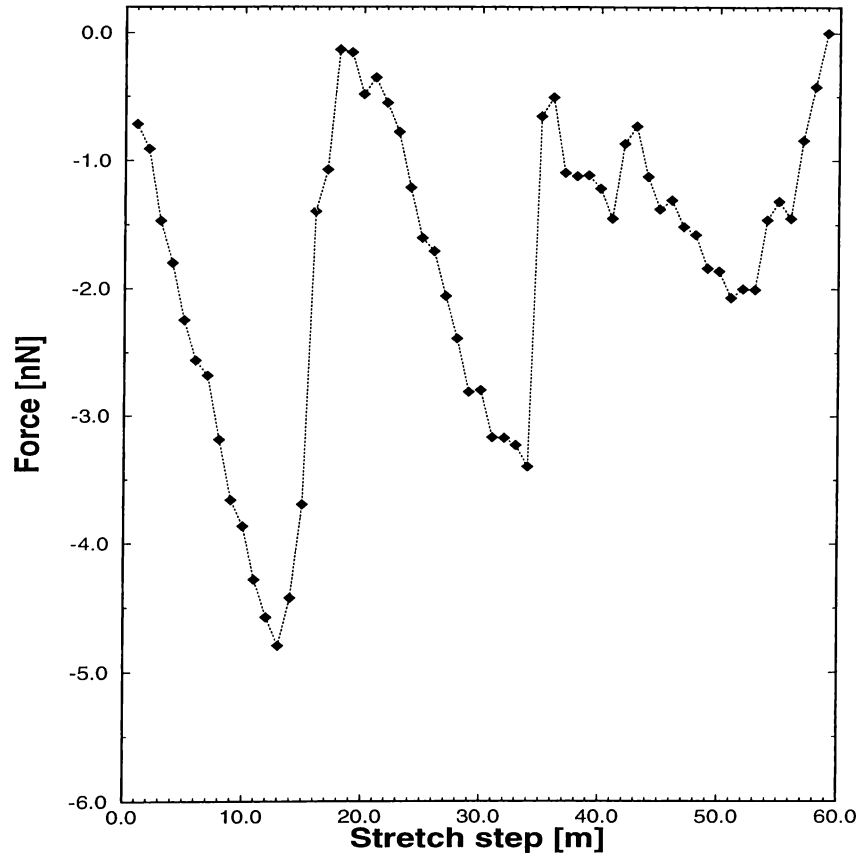


Figure 3.11: Force versus Stretch increment $m\Delta l$ for nanowire $WN3$ at $T = 300 K$.

each other and increase the force of attraction between them so that they can move from one local minimum to another.

3.3.4 Nanowires $WN3$

Finally we have investigated nanowire $WN3$. This correspond to a “wide-neck” $Cu(111)$ structure. This neck may show interesting features because it is known to be more stable compared with $Cu(100)$ structure. We made our simulation for $WN3$ at temperature $T = 300K$. We present our force plot $F_z(m)$ (for $WN3$) in Figure 3.10. Investigation of this plot, shows that the fluctuations in the force is minimized compared to the graphs for $WN1$ and $WN2$ structures. In this curve, we can recognize 4 jumps corresponding to $m = 18$, $m = 36$, $m = 43$

and $m \sim 58$ which correspond to the neck break. We note that the first two jumps correspond to subsequent stretches of the order of interlayer spacing in Cu(100) $\sim 1.8\text{\AA}$, but not in Cu(111) $\sim 2.1\text{\AA}$, while the third one corresponds to a stretch $\sim 0.6\text{\AA}$. From our previous analysis we conclude that it is very difficult to have any new layer formed during the third jump. After investigation of the side view, we understand that the first two jumps correspond to formation of a new layer with smaller cross-section (with 6 and 3 atoms) after amorphisity has occurred. However, the structure of the central region of the neck seems to be very unstable after the 2nd layer is introduced. From $m = 37$ up to $m = 41$, the layer structure in the central *four* layers has smeared out and we had to wait up to $m = 42$ in order to recover the structure with the same number of layers as in $m = 36$. Therefore, the third jump is just a sign of recovering layer structure with neck layers having atoms 5,3,3 and 7. This configuration also seems to be unstable, because there was a bouncing between the configuration with 3 atoms at the central layer and the one with only two atoms as a function of stretch until $m = 53$. After this point, the neck central region became amorphous and the neck was broken after few steps.

From the above discussion, we conclude that after stretch of $\sim 3.6\text{\AA}$, layer structure is not well defined at the central region. On the other hand, it is very stable at the 2 layers adjacent to *M* structure. This would suggest that the reason for the amorphisity in the central region is the diminishing of any bulk property which can keep the structure stable as a function of stretch. However, one may raise the point that we have already stretched the structure *WN1* for $\sim 5.5\text{\AA}$ and we have not seen this property. In fact, eventhough this point seems quite reasonable, we should emphasize that the original neck length for *WN3* nanowire is 6 Cu(111) layers. In the nanowire, *WN1*, we were using only 5 layers of Cu(100). This would yield to an increase of $\sim 3.7\text{\AA}$ in the *WN3* nanowire neck length which would result in a less bulk effect at the neck central region, and this is the reason for the amorphisity in the system. After this analysis, we have investigated the lateral structure in the layers once they occur. During the stretching process, the lateral atomic positions in every layer

formed a hexagonal shape or a portion of it. This was the original configuration given. Even the interatomic separation distance has increased slightly whenever atoms feel surface effect. In fact this hexagonal shape has already been observed in Cu(100) structure when the interlayer separation distance has increased. To understand this process better, we have made two different simulations. The first one containing 5Cu atoms and the second one having 7Cu atoms; and they were constrained to move on a plane. After convergence was reached, the 5Cu atom system has formed a portion of a hexagon while the 7 atom shape was a complete one. The interatomic separation distance was in the range of the nearest neighbor distance in Cu bulk material. It was in the range of $\sim 2.4 - 2.9\text{\AA}$. This result shows that that Cu(111) layer structure is the stable one. However, investigation of the layer positioning with respect to each other has shown that $A - B - C$ sequence is very fragile in the presence of surface effects. We have noticed that initial relaxation of the system was enough to destroy the closed packed form. In fact the hallow site configuration was the most preferable one, but it was made in a complete disorder. Due to this disorder in the layer positioning sequence, we expect some also variation in the interlayer distance (We expect it less than the original one since this configuration is similar to Cu(100)one). This would of course lead to a new layer induction even at early stage.

Now we would compare the early results obtained for nanowire $WN1$ and these ones. We conclude that the layer structure in Cu(111) is much more stable. However, due to surface effects, the layer sequence in these structures is very fragile and it seems that sequences obtained in Cu(100) are much more stable. However we note that the transition process for decreasing the contact area is random. This change can be even up to three atoms. It is also worth to note that, atom migration can also be important in decreasing the contact area but it has a minor effect on physical quantities because it occurs at wide crosssections and it corresponds to atoms at the surface.

Chapter 4

Self-Consistent-Field Pseudopotential Calculations

The electronic and atomic processes in nanowires have been treated in the previous chapters by using certain models and approximate methods. To confirm the results obtained from these studies and to examine certain features we need to carry out *ab - initio* calculations. For example, to better understand the conduction in an infinite atomic chain, we performed structure optimization by using total energy minimization, and carried out electronic structure as well as charge density calculations on various atomic chains formed from certain metal and semiconductor atoms. The *ab - initio* potential $V(\vec{r})$ was also of interest, to fit the potential in equation 2.23. To investigate the variation of this potential and compare with the infinite wall cylindrical potential, we also calculated $V(\vec{r})$ in atomic neck self-consistently. We also calculated the yield strength of atomic chain to understand the origin behind the observed yield strength.⁴¹⁻⁴³ The results of all these *ab - initio* calculations are combined to construct our theory on the electronic and atomic processes in nanowires.

We performed self consistent-field (SCF) pseudopotential calculations in the momentum space within local density approximation. We used nonlocal, norm conserving pseudopotential given by Bachelet *et. al.*⁵¹ The exchange-correlation potential is expressed by Wigner form. In many calculations, the atomic

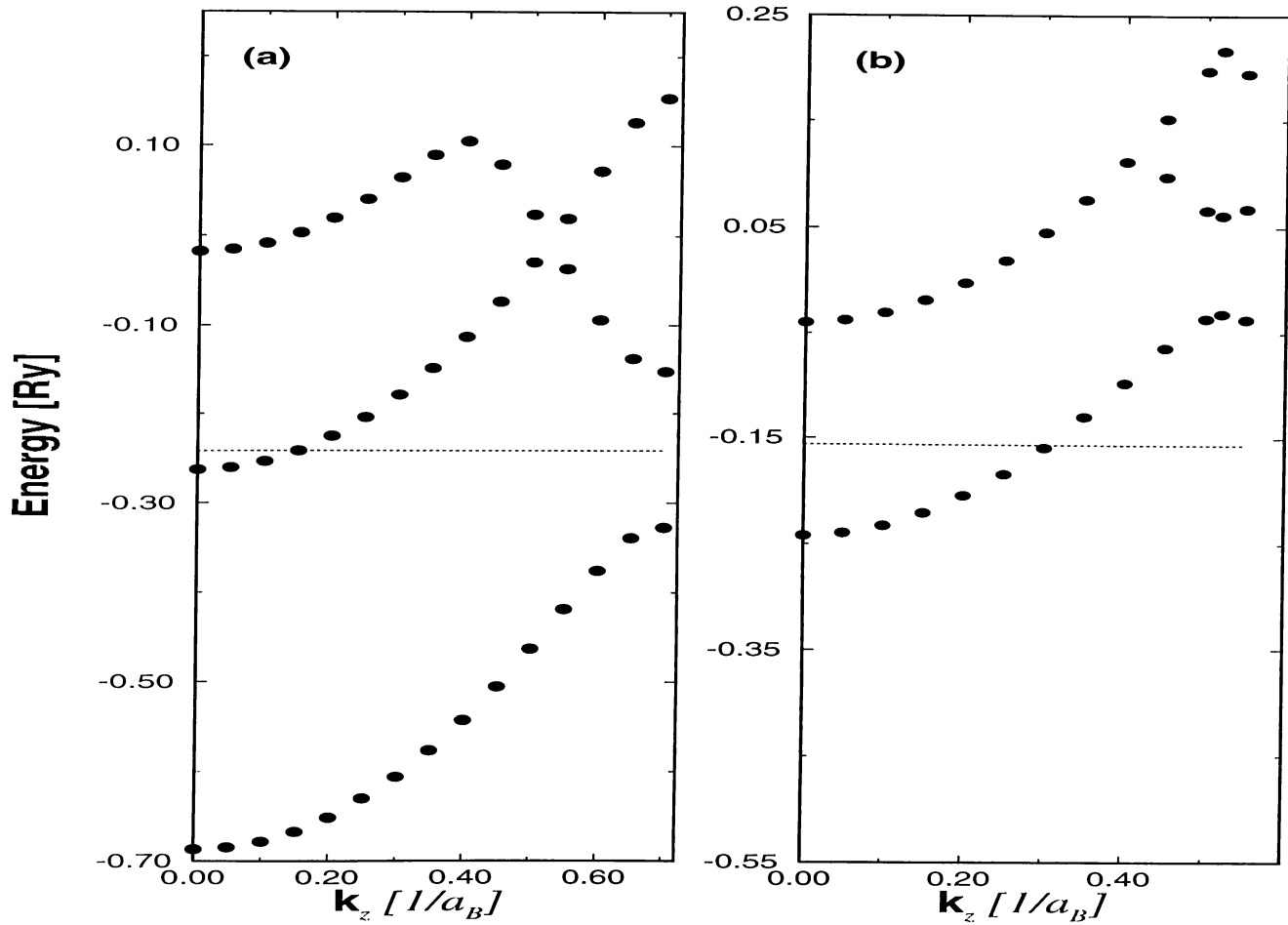


Figure 4.1: Band structure for an optimized *one* dimensional chain of Al(a), and Na(b) along k_z with k_x and k_y set to *zero*. The horizontal lines show the corresponding Fermi levels.

structure is optimized to have minimum total energy. In the calculations the self-consistency iterations are continued until mean-square difference between two consecutive iterations is smaller than $10^{-7} Ry$. In the band energy and charge density calculations the k -sampling is selected to yield convergent results. For Al and Na we used the kinetic energy cut-off $|\vec{k} + \vec{G}|^2 < 7.5 Ry$.

We computed first the total energy of the bulk Al and Na, to calculate the energies relative to the bulk values. We carried out calculations on the infinite Al and Na atomic chains with and without Peierls distortion, Al and Na neck having single atom, bulk and nanowire Young modulus.

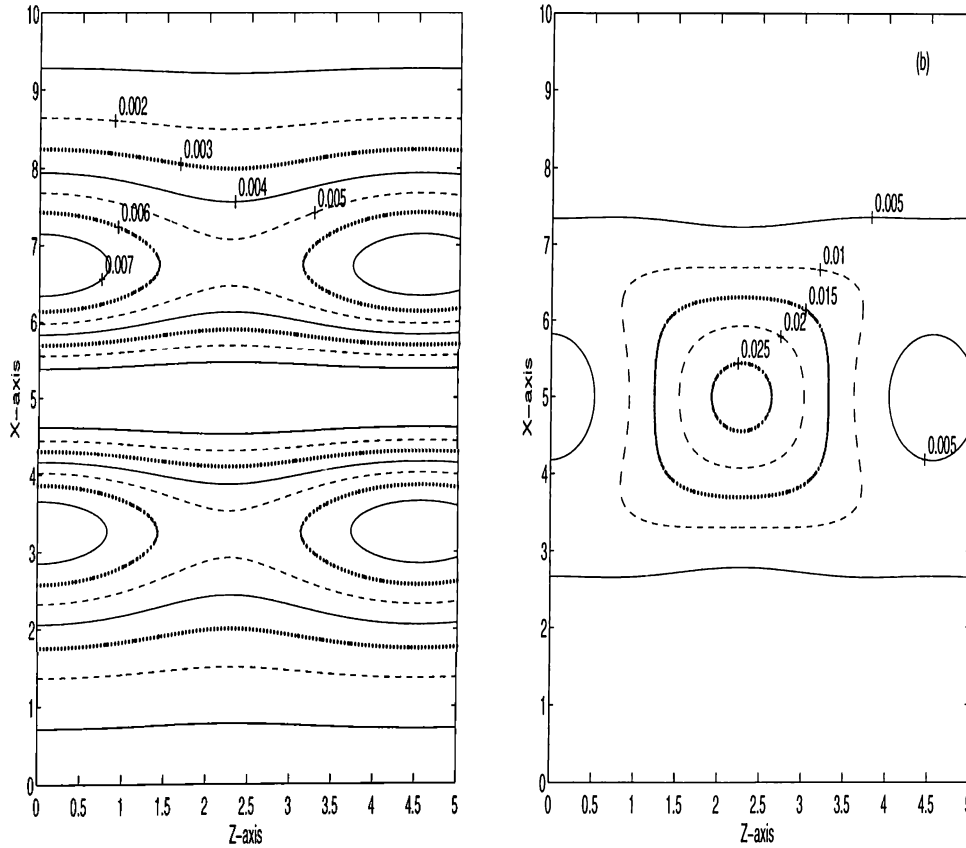


Figure 4.2: Probability wave function in 1D Al chain corresponding to $k_x = k_y = 0$ and $k_z = 0.2$. (a) for the second and the third band due to degeneracy, while (b) for the first band. Here the plot is along $x - z$ plane at $y = 0$, and the line with $x = 5$ corresponds to the chain.

In Figure 4.1, the electronic band structure of the Al and Na chains are shown. The binding energy of the Al-chain relative to Al bulk is $0.172Ry/atom$. From this result we understand that the Al-chain yields positive binding energy (or cohesion) which is slightly smaller than the bulk cohesion. The binding in Al-chain occurs by the σ -bond between $3p_z + 3s$ orbitals aligned along the chain axis. The $3p_x$ and $3p_y$ orbitals attribute to the cohesion by relatively weaker π -bonds. The widths of the $3sp\sigma$ and $3p\pi$ -bands are $\sim 0.4Ry$ and $\sim 0.2Ry$, respectively. The $3p\pi$ -band is degenerate and crosses the Fermi level. In Figure 4.2 we show the results for charge density distribution for state $k_x = k_y = 0$ and $k_z = 0.2$ and on the $x - z$ plane with $y = 0$. The first contour plot (a), correspond to the

state with $n = 2$ as well as the state with $n = 3$. This is due to the degeneracy in the $3p\pi$ -bands. In (b), we show the plots for $n = 1$. Analysis of these graphs indicates that the probability of the density of state with $n = 1$ is by a factor of 3 less than the one corresponding to state $n = 2$ and $n = 3$. Moreover, this state is nearly localized in the region intermediate between the two atoms whereas the others are extended along the chain direction. Due to these properties of states $n = 2$ and $n = 3$; we conclude that in $1D$ Al systems, 2 channels open for current carrying states and the conductivity would be $\sim 2 \times 2e^2/h$ whenever a small potential difference is applied between the ends.

We have also investigated Pierls distortion along the z - axis for Al structures and they have resulted in a much more stable structure than the $1D$ chain. However its binding energy was still less than the bulk Al cohesive energy as it is expected. We have investigated band structure along this system and its charge density distribution. The results were qualitatively the same as for the case of $1D$ chain. In fact, such a result is not surprising because such a distortion does not destroy the symmetry for $3p_x$ and $3p_y$ in the system and as a result the $3p\pi$ -bonding is still degenerate.

The Na-chain has only one band which crosses the Fermi level and it is half-filled. This band is mainly due to the bonding contribution of Na $3s$ orbitals. After investigating charge density distribution of this state on the $x - z$ plane we found that it is a conducting state in the z - direction. Therefore, this band contributes to one quantum conductance to the conduction along the chain. From these results we conclude that electronic properties of atoms at the contact play crucial roles in the conductance calculations. If these two problems were treated within free electron model they would apparently lead to the same result. In these treatments only the potential $V(\vec{r})$ is taken into consideration which was apparently the same for both of them. This potential contour plot was also investigated and it can be approximated well with an infinite wall cylindrical potential.

Following this study which has shown the importance of electronic structure, we were motivated to study some electronic characteristics of neck structures

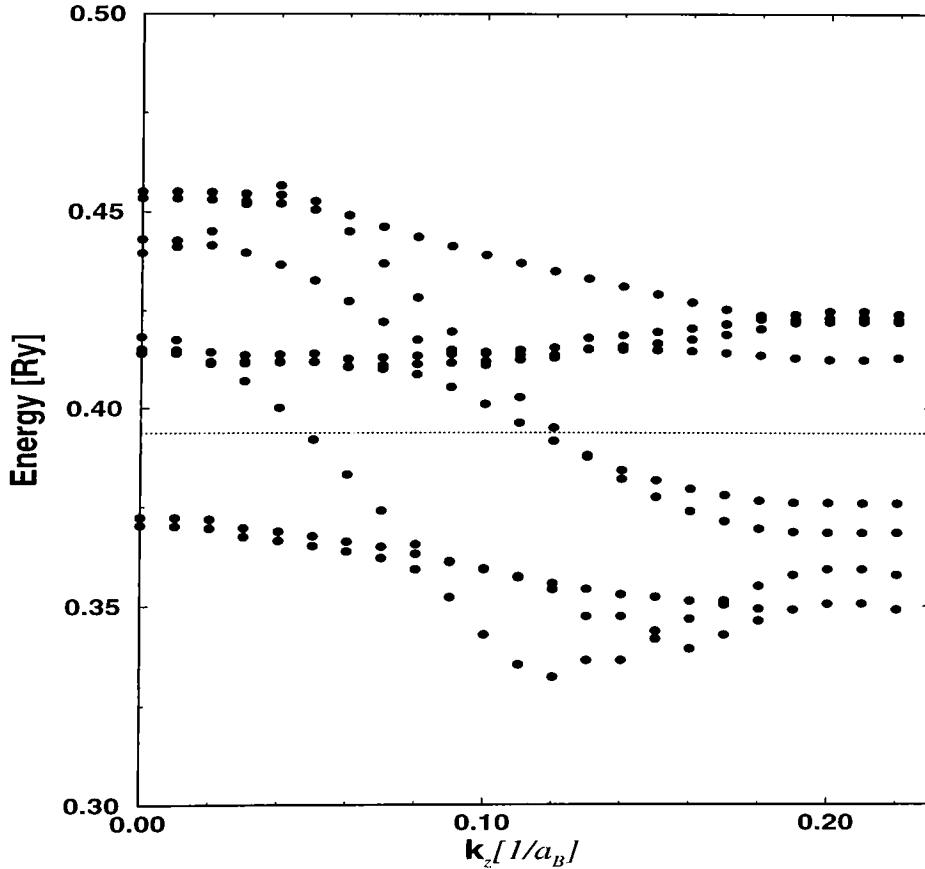


Figure 4.3: Energy band structure for Al neck along the k_z while $k_x = k_y = 0$. The bands are drawn from $n = 39$ until $n = 49$.

using SCF calculations. We have initially simulated one Al atom between two slabs. In this model we are representing the slabs by three layers of Al(100) surfaces. Each layer is composed of 9 atoms and the system is periodic in $3D$. We are in fact aware that this periodicity may include some artificial effect on the wave function solution. We are now still at the first steps for investigating this problem and we are increasing the dimensions for consistent results. After reaching convergence, we calculated the band structure along k_z direction while $k_x = k_y = 0$. These results are shown in Figure 4.3. In this figure there are many states that are crossing the Fermi level. At a first glance, one may think that our system is resulting in many conducting states and would lead a higher conductivity compared to Al-chain. Investigation of the probability

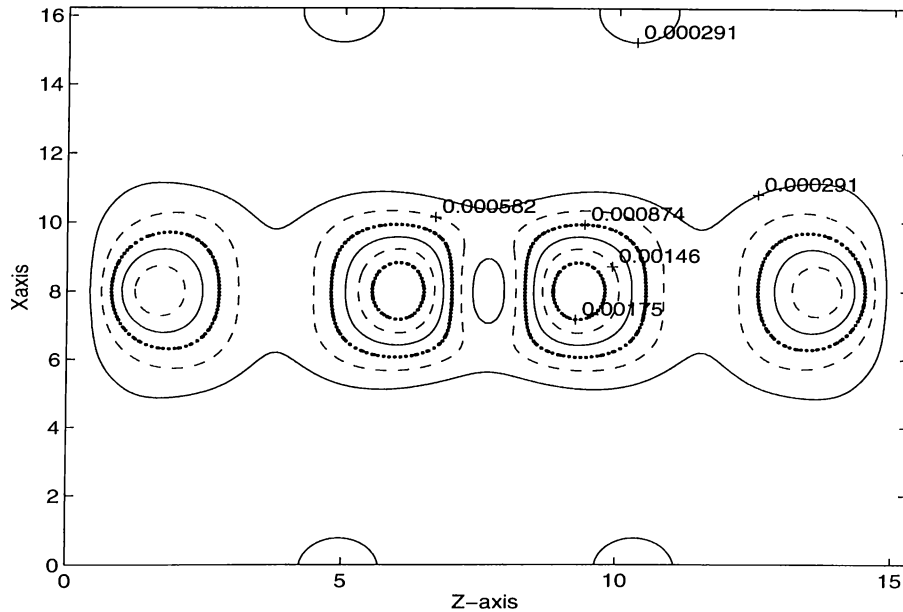


Figure 4.4: Probability density distribution of the 41st band and corresponding to $k_z = 0.05$ state.

density distribution of these states on the $x - z$ plane has shown that there is only one conducting state. The probability density for this state is shown in Figure 4.4. From these results, we recognize that the structure transformation leads to a different type of bonding and this may affect the result for conductivity calculation.

Finally, we wanted to investigate the yield strength in the 1D nanowires and compare it to the experimental value. In order to do this, we obtained the total energy of the system as a function of displacement of Al atoms from their equilibrium distance. This showed that for a small displacement $\sim 0.5\text{\AA}$, it is easy to make a parabolic fit, from which we deduced the spring constant of the 1D chain. Now we can calculate the Young's modulus defined by

$$Y = \frac{\text{stress}}{\text{strain}} = \frac{F/A}{\Delta L/L} \quad (4.1)$$

Now treating the force as the spring constant multiplied by the stretch increment, we found Young's modulus as 263.33GPa which is a value of *four* orders of magnitude larger compared to the average value for bulk Al. This shows that the

neck structure is very stable and resists any stretch before it breaks.

Chapter 5

Conclusion

In this work we investigate electronic and atomic properties of nanowires and atomic chains to understand electronic transport and fracture yielding mechanisms. Our aim is to develop a theory which resolve the dispute on the “quantization” of conductance in connective necks. We have based our study on experimental results taken by STM and MCBJ. In these works,²⁴⁻²⁷ conductance G is measured as a function of separation between two samples forming a neck. These results have revealed a step structure shape in G versus s curves, having step heights usually at multiples of $G_o = 2e^2/h$. However, the G versus stretch curve were not fully reproducible. Sometimes, they have small slopes (positive for the last plateau and negative at the intermediate stages). Moreover, we have noticed that at some circumstances dipping phenomenon occurs before formation of a new plateau (with smaller conductance). In view of those experimental results, it is concluded that the conductance is quantized in nanowires.^{17,23} It was also thought that treating these necks with free electron model in the ballistic regime would fully explain these results. In fact this type of approach is a generalization of conductance quantization phenomenon observed in *2DEG*. In this type of analysis, every energy eigenstate which dips below the Fermi level opens a new channel giving conductance $\sim 2e^2/h$. We have applied this type of formalism by solving Shrödinger equation in all space (treating the samples at the left hand side and right hand side with jellium approximation). After finding the wave function,

we have calculated the current passing through the constriction if a very small chemical potential difference $\Delta\mu$ is applied between the left and right electrodes. Then we have calculated the conductance as a function of cross-section of the constriction. These calculations were carried out by approximating the potentials with circular symmetry, which comprise both infinite cylindrical potential well and parabolic potential. Some qualitative features were obtained while comparing these results with experimental ones; at least the step structure has appeared. However, all other experimental features were absent. Therefore, we generalized our method to a much more realistic potential and we made simulation of pushing a tip into a jellium slab. The results were also featuring only few aspects of the experimental data and steps were not very sharp when G versus s curve was plotted. This has made us convinced that treating the problem within the free electron model does not include all aspects of the experiments, and probably investigating the idea that relates the variation of conductance to atomic rearrangement may lead to better results.

To investigate the atomic rearrangement, we have simulated different neck structures with Molecular Dynamics method for different parameters, such as size, temperature, stretch speed etc. The general results obtained were qualitatively the same; and in the following part we present the most interesting aspects obtained and relate them to experimental results.

- As a function of pulling, the neck conserves its atomic structure for a long time. Once the length of the stretch becomes approximately equal to the interlayer spacing, a new layer with smaller cross-section is induced at the center of the neck. This change occurs at a very short time scale and it is followed by a similar sequence until the next layer is formed.
- Every change in cross-section corresponds to an abrupt jump in the attractive force between the top fixed layers and the rest of the system (tip and sample). This is in agreement with recent experiments which measure the variation of conductance and force simultaneously.⁴¹⁻⁴³
- The theoretical results together with the recent experimental results

show that the change in conductance measurement is due to atomic rearrangement; as the new layer with smaller crosssection is formed, the conductivity drops to a lower plateau.

- The change in the contact area is not constant, therefore the step height in the conductivity may change and it is dependent partly on the conditions of the experiment and partly chaotic.
- After a new layer is formed, we have noticed that number of atoms contained in this layer may increase. This may result in variation of G in the same plateau.
- Atoms which are occurring at the neck surface migrate; this would also change the conductivity slightly and may result in a negative slope in the plateau of conductivity.
- Our simulation showed that in the last configuration, we may have *one* or *two* or even *three* atoms before the neck breaks. Therefore it is becoming very difficult to talk about any universality for these problems.
- In our simulation a bundle form appears just before the neck breaks. This bundle shape is improving as a function of neck stretch and this would result in a positive slope for the last plateau of conductivity.

In addition to this work, we have also made some *ab - initio* calculations to investigate the electronic and atomic structure of nanowires and atomic chain. These have shown that in small scale structures where the energy of states become discrete, electronic structure play a crucial role in conductivity calculations. For example Na 1D chain contributes to a conductivity $\sim 2e^2/h$ while that of Al contributes $\sim 4e^2/h$. Furthermore, the atomic structure at the neck and its crosssection to the rest of the electrodes are crucial in the resetting of electronic structure and transport properties. This implies that a realistic solution of the problem has to consider the full atomic structure together with the true connection to the reservoirs.

Finally, we also predicted that an atom chain has a Young modulus much larger than the bulk value. Therefore, we believe that a good understanding of the problem requires treating all three phenomena, namely, free electron model, atomic and electronic structure, simultaneously.

Bibliography

- [1] P. W. Anderson, Phys. Rev. 109, 1492(1958)
- [2] U. Landman, W. D. Luedtke, N. A. Burnham, R. J. Cotton, Science 248, 454(1990)
- [3] J. K. Gimzewski and R. Möller, Phys. Rev. B41, 2763(1987); J. K. Gimzewski, R. Möller, D. W. Pohl, R. R. Schlitter, Surface Science 189, 15(1987); J. K. Gimzewski and D. W. Pohl, Phys. Rev. Lett. 57, 2403(1986)
- [4] B. J. van Wees, H. van Houten, C. W. J. Beenakker, J. G. Williamson, L. P. Kouwenhoven, D. van der Marel and C. T. Foxon, Phys. Rev. Lett. 60, 848(1988)
- [5] D. A. Wharam, T. J. Thornton, R. Newbury, M. Pepper, H. Ahmed, J. E. Frost, D.G. Hasko, D. C. Peacock, D. A. Ritchie and G. A. C. Jones, J. Phys. C21, L209(1988)
- [6] Yu V. Sharvin, Soviet Physics-JETP21, 655(1965)
- [7] G. Timp, A. M. Chang, P. Mankiewich, R. Behringer, J. E. Cunningham, T. Y. Chang and R. E. Howard, Phys. Rev. Lett.59, 732(1987)
- [8] R. Landauer, IBM J. Res. Dev.1, 223(1957)
- [9] G. Kirczenow, Solid State Comm. 68, 715(1988)
- [10] A. Szafer and A. D. Stone, Phys. Rev. Lett. 62, 300(1989)

- [11] N. Garcia and L. Escapa, *Appl. Phys. Lett.* 54, 1418(1989)
- [12] E. G. Hanappel and D. van der Marel, *Phys. Rev.* B39, 5484(1989)
- [13] E. Tekman and S. Ciraci, *Phys. Rev.* B39, 8772(1989); E. Tekman and S. Ciraci, *Phys. Rev.* B43, 7145(1991).
E. Tekman, PhD thesis, Bilkent University, (1990)(Unpublished)
- [14] M. Yosefin and M. Kaveh, *Phys. Rev. Lett.* 64, 2819(1990)
- [15] G. Kirczenow, *Phys. Rev.* B39, 10452(1989)
- [16] M. Büttiker, Y. Imry, R. Landauer and S. Pinhas *Phys. Rev.* B31, 6207(1985)
- [17] N. Garcia, STM'87 Conference held at Oxnard, California(1987)
- [18] N. D. Lang, *Phys. Rev.* B36, 8173(1987)
- [19] J. Ferrer, A. Martin-Rodero and F. Flores, *Phys. Rev.* B38, 10113(1988)
- [20] S. Ciraci and E. Tekman, *Phys. Rev.* B40, 11969(1989)
- [21] N. Agrait, J. G. Rodrigo, and S. Vieira, *Phys. Rev.* B47, 12345(1993)
- [22] J. I. Pascual, J. Méndez, J. Gómez-Herrero, A.M Baró, V. T. Binh, *Phys. Rev. Lett.* 71, 1852(1993)
- [23] L. Olesen, E. Laegsgaard, I. Stensgaard, F. Besenbacher, J. Schiøtz, P. Stoltze, K. W. Jacobsen and J. K. Nørskov, *Phys. Rev. Lett.* 72, 2251(1994)
- [24] J. I. Pascual, J. Méndez, J. Gómez-Herrero, A.M Baró, N. Garcia, U. Landman, W. D. Luedke, E. N. Bogachek, H. P. Cheng, *Science* 267, 1793(1995)
- [25] J. M. Krans, C. J. Müller, I. K. Yanson, T. C. M. Govaert, R. Hesper, J. M. Van Ruitenbeck, *Phys. Rev.* B48, 14721 (1993)
- [26] J. M. Krans, J. M. Van Ruitenbeck, *Phys. Rev.* B50, 17659(1994)

- [27] J. M. Krans, J.M Van Ruitenbeck, V. V. Fisun, I. K. Yanson, L. J. de Jongh, Nature 375, 767(1995)
- [28] C. J. Muller, J. M. van Ruitenbeek and L. J. de Jongh, Phys. Rev. Lett. 70, 2138(1993)
- [29] T. N. Todorov and A. P. Sutton, Phys. Rev. Lett. 70, 2138(1993)
- [30] D.M Newns, Phys. Rev. 178, 1123(1969)
- [31] Torres, J. A. Pascual and J. I. Sáenz, Phys. Rev. B49, 16581(1994)
- [32] J. M. Krans, C. J. Müller, N. Van der Post, F. R. Postama, A. P. Sutton, T. N. Todorov, and J. M. Van Ruitenbeck, Phys. Rev. Lett. 74, 2146(1995); L. Olesen, E. Laegsgaard, I. Stensgaard, F. Besenbacher, J. Schiøtz, P. Stoltze, K. W. Jacobsen and J. K. Nørskov, Phys. Rev. Lett. 74, 2147(1995)
- [33] B. J. Alder and T. E. Wainwright, J. Chem. Phys. 27, 1208(1957)
- [34] S. Ciraci and E. Tekman, Phys. Rev. B40, 11969(1989); S. Ciraci, Tip-surface interactions in Scanning Tunneling Microscopy and Related Methods edited by R. J. Bohm, N. Garcia and H. Rohrer, page 113 Kluwer Academic Publishers Volume 184(1990)
- [35] Y. Imry, In directions in condensed matter physics:101-163, World Scientific Press, Singapore(1986)
- [36] M. Büttiker, I.B.M Journal of Research and Development 32, 317(1988)
- [37] M. Büttiker, Phys. Rev. B35, 4123(1987)
- [38] A. M. Bratkovsky, A. P. Sutton and T. N. Todorov, Phys. Rev. B52, 5036(1995)
- [39] I. Kander, Y. Imry and U. Sivan, Phys. Rev. B41, 12941(1990)
- [40] U. Landman, W. D. Luedtke, N. A. Burnham, R. J. Calton, Science 248, 454(1990) ; U. Landman and W. D. Luedke, J. Vac. Sci. Technol. 9, 414(1991)

- [41] N. Agrait, G. Rubio and S. Vieira, *Phys. Rev. Lett.* 74, 3995(1995)
- [42] A. Stalder and U. Dürig, *Appl. Phys. Lett.* 68, 637(1996)
- [43] G. Rubio, N. Agrait and S. Vieria, *Phys. Rev. Lett.* 76, 2302(1996)
- [44] Uzi Landman, W. D. Luedtke, Brian E. Salisbury and Robert L. Whetten,
(to be published)
- [45] M. S. Daw and M. I. Baskes, *Phys. Rev.* B29, 6443(1984)
- [46] S. M. Foiles, M. I. Baskes and M. S. Daw, *Phys. Rev.* B33, 7983(1986); See
also Errata, *Phys. Rev.* B37, 10378(1988)
- [47] M. S. daw, *Phys. rev.* B39, 7441(1989)
- [48] Ş. Erkoç, *Z. Phys.* D32, 257(1994)
- [49] J. H. Rose, J. R. Smith, F. Guinea and J. Ferrante, *Phys. Rev.* B29,
2963(1984)
- [50] S. Ciraci, E. Tekman, A. Baratoff and I. P. Batra, *Phys. Rev.* B.46,
10411(1992)
- [51] G. B. Bachelet, D. R. Hamann and M. Schlüter, *Phys. Rev.* B26,
(4199)(1982)